Advanced green peel utilization for efficient methylene blue removal: Integrated analysis and predictive modeling

Oumnia Rayane Benkouachi, Abdallah Bouguettoucha, Hichem Tahraoui, Abderraouf Guediri, Derradji Chebli, Mohammed Kebir, Salah Knani, Jie Zhang, Abdeltif Amrane

Advanced Green Peel Utilization for Efficient Methylene Blue Removal: Integrated Analysis and Predictive Modeling

Oumnia Rayane Benkouachi [1], Abdallah Bouguettoucha [1], Hichem Tahraoui [1,2,3], Abderraouf Guediri[1], Derradji Chebli [1], Mohammed Kebir [4,5], Salah Knani [6], Jie Zhang [7], and Abdeltif Amrane [3, *]

[1] Laboratory of Chemical Process Engineering, Department of Process Engineering, University of Ferhat Abbas, Setif 19000, Algeria.

[2] Laboratory of Biomaterials and Transport Phenomena, University of Médéa, Médéa 26000, Algeria

[3] Univ Rennes, Ecole Nationale Supérieure de Chimie de Rennes, CNRS, ISCR – UMR6226, F-35000 Rennes, France.

[4] Research Scientific and Technical Center on Physico-Chemical Analysis (CRAPC), Industrial Zone Bou-Ismail, Tipaza, Algeria.

[5] Unite Research in Physical and Chemical Analysis on Fluid and Solid Medium (UR-APC-MFS/CRAPC),11 Road Doudou Mokhtar, Ben Aknoun, Algiers, Algeria.

[6] Department of Physics, College of Science, Northern Border University, Arar, Saudi Arabia.

[7] School of Engineering, Merz Court, Newcastle University, Newcastle upon Tyne NE1 7RU, UK.

* Correspondence: E-mail: Abdeltif.amrane@univ-rennes1.fr

Abstract

This study explores the adsorption of Methylene Blue (MB) onto Green Peel (GP) material, utilizing advanced analytical techniques and modeling approaches. Fourier-transform infrared spectroscopy (FT-IR) confirms GP's effectiveness as an adsorbent. The study systematically examines the influence of key factors such as adsorbent dose, pH, MB concentration, and temperature on adsorption efficiency. Among the isotherm models analyzed, the monolayer with double energy (M2) model is identified as the most accurate for describing MB adsorption onto GP. Steric parameters provide insights into the adsorption mechanism, revealing temperature-dependent changes. Thermodynamic analysis indicates an exothermic adsorption process, with a decrease in adsorption capacity at elevated temperatures. Density Function Theory (DFT) analysis highlights the potential for electron transfer during adsorption, contributing to a deeper understanding of the process. Molecular Dynamic Simulation (MDS) uncovers stable adsorption configurations and reveals the significance of chemical interactions and Van der Waals forces. Gaussian Process Regression with Lévy Flight Distribution (GPR_LFD) demonstrates exceptional predictive accuracy, closely aligning experimental and predicted MB uptake values. Optimal adsorption conditions (30 minutes contact time, 0.6 g adsorbent dose, 400 mg/L initial MB concentration, pH 6.6, and 10°C) yield an adsorption capacity of 207.90 mg/g. The integration of LFD optimization and GPR prediction through a MATLAB interface further enhances the practical application of these findings. This comprehensive investigation not only advances the understanding of MB adsorption onto GP but also highlights GP's potential as an efficient, reusable adsorbent.

Graphical Abstract:

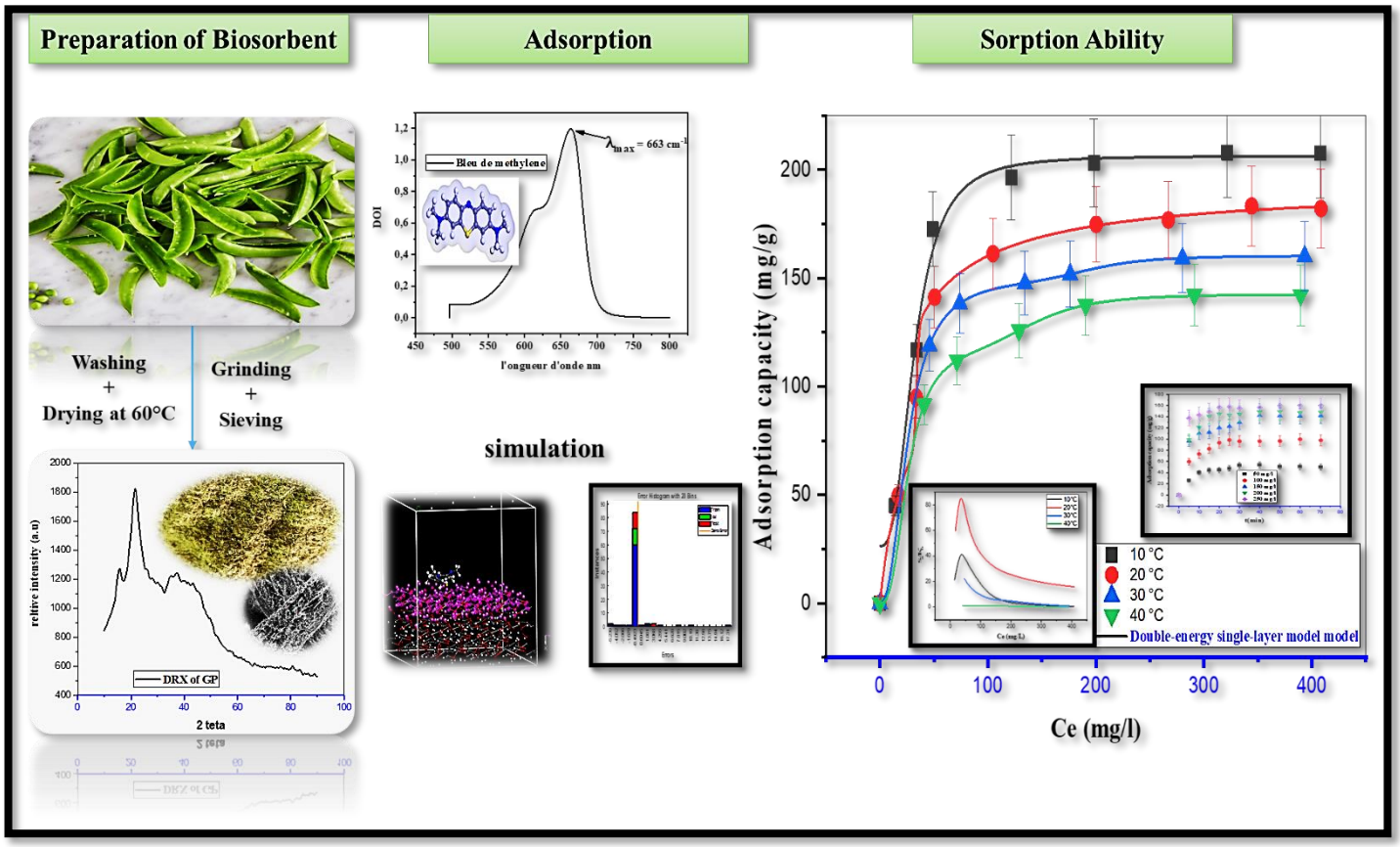

Keywords: Adsorption, Green peas, Methylene blue, density functional theory, Gaussian Process Regression, Lévy Flight Distribution.

1. Introduction

Industrial effluents from various industrial sectors, including textiles, dyeing, food processing, pharmaceuticals, paper manufacturing, leather production, and cosmetics, serve as a prominent source of environmental pollution and are notable generators of chromatic wastewater emissions [1–3]. Among these sectors, the dye industry plays a notably pivotal role in this environmental context. [4,5]. Dye compounds in water hinder sunlight penetration, disrupting aquatic plant photosynthesis and posing serious health risks due to their mutagenic, carcinogenic, and teratogenic properties, which can harm human kidneys, liver, reproductive system, and central nervous system [6–9]. Untreated wastewater containing dyes like

Methylene Blue, a chemically stable and water-soluble cationic dye, poses significant environmental risks due to its persistence and widespread industrial use [10]. The release of this dye into the environment causes serious health issues, including nausea, respiratory problems, allergic reactions, cardiac arrhythmias, tissue necrosis, cognitive impairment, cancer risks, and dysfunction in the brain, liver, and central nervous system [11,12]. Our previous studies conclude that the biomass was ineffective in removing anionic azo dyes. The negatively charged surface and open structure of the GP adsorbent likely contribute to its low adsorption performance. Throughout the years, researchers have effectively devised a diverse array of methodologies for the eradication of methylene blue in industrial effluent, including electrochemical treatment, ion exchange, photocatalytic degradation [13], membrane filtration, coagulation-flocculation [14,15], and Fenton process [16,17]. Among these techniques, the adsorption method is an important process for improving the quality of water and protecting the environment [4,18]. Due to its is an efficient, simple, regenerable, and eco-friendly method for treating wastewater and reducing hazardous pollutants. [19,20].

Various adsorbents, including those made from agricultural and industrial byproducts, offer a straightforward, cost-effective, and eco-friendly solution for dye removal. Using these raw adsorbents helps reduce waste disposal costs and addresses environmental challenges. Modifications are needed to enhance their practical use and improve their adsorption efficiency, durability, and reusability [9]. Different modifying reagents, such as base solutions (sodium hydroxide, calcium hydroxide, and sodium carbonate) and mineral and organic acids (hydrochloric acid, sulphuric acid, nitric acid, tartaric acid, thioglycolic acid, citric acid, etc.), are used in the chemical modification of adsorbents [21].

Researchers have conducted extensive examinations and assessments of prospective biosorbents in order to successfully extract colors from water pollution.

In recent years, notable advancements have included the utilization of materials such as orange peel [22], Ziziphus jujube [23], Pinus pinaster [24], almond shell [25], Acorus calamus [26], green macroalgae [27], the prickly pear [28], corn cob [29], and other similar substances for various successful applications in dye removal processes.

Despite advancements in adsorption methods, several limitations persist [30]. The limited adsorption capacity of traditional adsorbents can be quickly exhausted, hindering their long-term effectiveness [31]. Additionally, the efficiency of adsorption can be compromised by inefficient processes, suboptimal conditions, and sometimes inadequate selectivity, leading to the adsorption of non-targeted components [31]. The development of new, efficient adsorbents remains a challenge, as does the optimization of operational conditions to ensure effective adsorption in variable environments [30].

To address these existing challenges, researchers have adopted artificial intelligence (AI) and optimization techniques using metaheuristic algorithms in the field of adsorption. Noteworthy studies include the development of AI-based models for predicting vanadium adsorption onto activated carbon nanocomposites [32], the application of AI modeling and genetic algorithm optimization for the decolorization of bromo-cresol green dye using acid-functionalized rice husk [33], and the utilization of deep learning and AI tools for modeling a pressure swing adsorption unit [34]. Additionally, researchers have explored the use of activated carbon derived from jujube pebbles for the adsorption of methylene blue, employing responsive surface methods, machine learning techniques, thermodynamics and mechanism analysis, modeling of kinetics and isotherms, and optimization [30]. Another study proposes a predictive model combining K-Nearest Neighbor with the Gray Wolf Optimizer Algorithm (KNN_GWO) for estimating the amount of phenol adsorption on powdered activated carbon [31]. Another study utilized artificial intelligence, specifically Gaussian process regression (GPR) and particle swarm optimization (PSO), to predict the adsorption capacity of MB dye and optimize the

treatment conditions of textile wastewater. These AI techniques are applied to enhance the efficiency of the treatment process by providing accurate predictions and identifying optimal operating conditions [35]. These approaches showcase the diverse applications of AI in optimizing adsorption processes.

The use of AI has allowed for precise identification of optimal conditions to maximize adsorption capacity, improve overall efficiency, and design selective adsorbents [30]. Moreover, AI has guided the virtual development of new adsorbent materials. Metaheuristic algorithms have been leveraged to optimize operational parameters, effectively explore the space of process operating conditions, dynamically regulate in response to load fluctuations, and provide accurate predictions of adsorption performance [31].

In the context of this study, the utilization of green peel (GP) was meticulously investigated as an adsorbent for the effective removal of methylene blue (MB) dye from solution-made water. In the early stages, scanning electron microscopy (SEM) and Fourier-transform infrared spectroscopy (FT-IR) were judiciously employed to confirm the dye adsorption process of GP. Conversely, X-ray diffraction (XRD) was specifically utilized to elucidate the crystalline structure of GP, offering crucial insights into the structural properties of the adsorbent material. The Brunauer-Emmett-Teller (BET) theory is widely used to analyze the surface area and porosity of materials

A systematic exploration of parameters influencing MB removal, including adsorbent mass, pH, initial concentration, and temperature, was conducted. Detailed analysis of isotherm data, accompanied by steric parameters, provided insights into the geometry and adsorption mechanisms. Furthermore, a comprehensive investigation into the reactivity and stability of MB and GP was undertaken, shedding light on potential electron transfer phenomena during the adsorption process. In the context of MB adsorption onto cellulose-based materials like green peel, diverse mechanisms contribute to the overall adsorption process. Notably,–MB

adsorption onto Green Peel (GP) involves multiple interactions, including electrostatic attraction, van der Waals forces, hydrogen bonding, and, under certain conditions, covalent bonding. Precipitation of MB onto GP occurs when concentrations exceed solubility, contributing to overall adsorption. The significance of each mechanism depends on factors like pH and temperature. GP's recyclability was confirmed using a 0.1 M ethanol solution, demonstrating its potential for reuse after evaluating removal efficiency and adsorption capacity. A dive into the stable adsorption configuration of MB on the GP surface through molecular dynamics simulation was undertaken. Simultaneously, a model based on the Gaussian process coupled with Levy flight distribution (GPR_LFD) was developed to predict MB adsorption by GP. Furthermore, Levy flight distribution (LFD) was independently used to identify optimal conditions for maximal MB removal. Finally, a user-friendly MATLAB interface integrating LFD optimization and GPR_LFD prediction was designed to facilitate the practical application of the obtained results.

Additionally, the study innovates by exploring the complex mechanisms of adsorption between GP and MB, using kinetic and adsorption models, as well as techniques like molecular mechanics and Density Functional Theory (DFT) simulation to provide critical insights into the underlying interactions. The development of an advanced prediction model based on GPR_LFD represents a major breakthrough, delivering highly precise estimates of GP's maximum adsorption capacity. In this investigation, the research stands as a pioneering contribution to the field of water treatment. By integrating innovative adsorbent materials, comprehensive characterization techniques, and advanced simulation tools, significant strides have been made in addressing water contamination issues caused by cationic dyes.

2. MATERIAL AND METHODS

2.1. Adsorbate used

To assess the adsorption capacity of the prepared biomass, a persistent and stable dye was chosen. MB was selected due to its reputation for persistence in various environments. Additionally, MB exhibits stability, ensuring the maintenance of its chemical and physical properties under variable conditions. These characteristics have made MB an ideal candidate to evaluate the adsorption efficiency of our biomass on a persistent contaminant. The characteristics of MB are detailed in **Table S1**, with the molecular structure depicted in **Figure S1.**

2.2. Preparation of solution

1 g of MB powder provided by the company SIGMA-ALDRICH was dispersed in 1 liter of distillate water to produce 1 g/L colorant solution. Then, various solutions ranging from 100 to 600 mg/L were made using distillate water. These solutions were then applied to various experiments.

A study of its visible UV spectrum at wavelengths between 200 and 800 nm, carried out using a UV-1700 type spectrophotometer pharmaspec Shimadzu, made it possible to determine the wavelength corresponding to the maximum absorbance, $\lambda max = 663$ nm.

2.3. Adsorbent preparation

GP were collected from residues of local green peas. After initial cleaning with distilled water and drying at ambient temperature, the material was pulverized, rinsed, and dried overnight in a furnace at 60°C to create natural biosorbents. Subsequently, preliminary trials were conducted to select the optimal material among the natural biosorbent, the one activated by orthophosphoric acid (GP-H_3PO_4), and the one activated by KOH (GP-KOH). Results indicated that the natural biosorbent removed 80% of MB, while the activated biosorbents (GP-KOH and GP-H_3PO_4) showed removal rates ranging from 69.17% to 28.14%. These outcomes prompted the selection of natural biomass as the preferred adsorbent for further research.

2.4. Characterization of adsorbent

In the current investigation, a range of characterization techniques was applied and will be elaborated upon later in this study. In particular, infrared spectroscopy was employed to scrutinize the surface chemistry of various specimens, including raw GP and GP loaded with methyl blue (GP+MB). This analysis was carried out using a Fourier transform infrared spectrometer (FT-IR) of the SHIMADZU brand, specifically an IRAffinity-1S model, in conjunction with potassium bromide (KBr) discs, within a spectral range spanning from 4000 to 500 cm^{-1}.

X-ray diffraction (XRD) diagrams were constructed in a 2θ angle range spanning from 4 to 90 degrees, with an incremental step of 0.02 degrees and an acquisition time of 6.985 seconds per step. To probe the micromorphology of the untreated green peel, a Hitachi S-3000N Scanning Electron Microscope (SEM) was utilized for image capture at electron beam energies of 10 kV and magnifications of 30, 100, and 300.

The scanning electron microscope (SEM) is considered a highly valuable tool for the examination and analysis of microstructural morphology. SEM relies on electron-material interactions to generate high-resolution images of the sample's surface. This technique was employed to scrutinize the surface characteristics and morphological attributes of the green peel (GP) samples under investigation.

The specific surface area of GP was calculated by using the Brunauer–Emmett–Teller (BET) method based on the data of the N2 adsorption–desorption isotherm.

The concept of the zero-point charge is a pivotal concept in physics, elucidating the circumstances surrounding the neutral electrical charge state of certain particles. This concept is founded on the fundamental premise that all matter inherently possesses an intrinsic level of energy, even in a state that may superficially appear at rest. This energy, recognized as "zero-

point" or "vacuum" energy, holds the potential to initiate interactions among particles, thereby leading to the acquisition of a net electric charge.

In the pursuit of determining the point of zero charge (pHpzc), a method was employed wherein 50 mL of sodium chloride (NaCl) solution was placed within sealed vials. The pH levels of these solutions were systematically adjusted across a range from 2 to 12 through the utilization of either a 0.1 M sodium hydroxide (NaOH) or 0.1 M hydrochloric acid (HCl) solution. Each vial was supplemented with 15 mg of GP material. Subsequently, the suspensions underwent agitation at ambient room temperature for an approximate duration of 24 hours, following which the final pH values were ascertained.

2.5. Effect of process variables on the adsorption process

2.5.1. The effect of biosorbent dose

One key element in figuring out the biosorbent material's potential for biosorption is the fraction of biosorbent in the solution. Adsorbent dosages of 0.2, 0.4, 0.6, 0.8, and 1 g/L were tested at an initial dye concentration of 100 mg/L to examine the impact of the initial dosage of GP biosorbent on the MB dye.

2.5.2. Effect of initial pH

Due to its ability to modify the surface characteristics of materials and affect the arrangement of anions and cations, pH is crucial to adsorption. In order to investigate the impact of pH on our experimental setup, a series of tests were conducted. namely, contacting a volume of 25 mL of MB in 100 mL Erlenmeyer flasks with 15 mg of green pea material (GP) and an initial concentration of 100 mg/L. These suspensions were initiated at distinct initial pH values implied from [2, 4, 6, and 10] and maintained at room temperature. The mixtures were subjected to agitation for 24 hours at a rate of 250 ppm. Following this, the suspensions underwent

centrifugation, and the ultimate concentration of filtrate was determined using ultraviolet (UV) spectroscopy.

2.6. Adsorption analysis

2.6.1. Adsorption kinetics

Studying adsorption kinetics is a critical phase in the analysis of an adsorption method as it facilitates the assessment of the duration necessary to reach adsorption equilibrium [36].

A range of distinct initial concentrations, represented by 50, 100, 150, 200, and 250 mg/L, were employed in the formulation of solutions. For each of the above concentrations of MB, 0.015 g of biosorbent material was introduced into 25 mL of a methyl blue solution in a 50 mL volumetric flask under continuous stirring at a speed of 250 rpm. At specific time intervals, samples were extracted for subsequent analysis using a Shimadzu Spectrophotometer UV-1700. Kinetic modeling plays a crucial role in the design of adsorption systems, and the quantity of adsorbate captured is computed using Equation (1) [37,38]

$$\boldsymbol{Q_t = \frac{(C_o - C_t)V}{m}} \quad \textbf{(1)}$$

Where C_o ($mg.L^{-1}$) is the first concentration of colorant, C_t ($mg.L^{-1}$) is the remaining concentration of dye at the time t, V (mL) is the volume of the solution, and m(g) is the mass of the adsorbent [39].

The dye clearance efficiency was determined using Eq. (2) [40]:

$$\mathbf{R\%} = \frac{C_o - C_e}{C_o} * \mathbf{100} \quad \textbf{(2)}$$

2.6.2. Kinetic modeling

The kinetics of solute adsorption were characterized using an adsorption dynamics study, which governed the rate of adsorption at the solid-solution interface. To fit the experimental data,

numerous kinetic models were used, including pseudo-first-order (PFO), pseudo-second-order (PSO), pseudo-nth-order (PNO) and Elovich models [41]. To identify the adsorption mechanism for design purposes, we used the intraparticle diffusion model [23,36], and the Fractional power kinetic model [42,43]

Table.1. Equation and parameters models for nonlinear regression of Kinetic adsorption.

Equation number	Equation name	Equation formed	Parameters
(3)	pseudo-first-order (PFO)	$Q_t = Q_e\,(1 - e^{k_1 t})$	**Q_e** (mg g^{-1}) and Q_t (mg g^{-1}) refer to the amount of dye adsorbed at equilibrium and at time t (min). respectively. **k_1**(L min^{-1}) is the equilibrium rate constant of the pseudo-first-order equation
(4)	pseudo-first-order (PSO)	$Q_t = \left(\frac{K_2\,Q_e^2\,t}{K_2\,Q_e\,t + 1}\right)$	**k_2** (L min^{-1}) is the equilibrium rate constant of the pseudo-second-order equation
(5)	pseudo-nth-order (PNO)	$Q_t = Q_e - \left[(n-1)K_n\,t + Q_e^{(n-1)}\right]^{1/(1-n)}$	**k_n** is a constant and n is the biosorption reaction order.
(6)	Elovich	$Q_t = \frac{1}{\beta}\ln(\alpha\beta) + \frac{1}{\beta}\ln t$	**α** is the constant of the initial sorption rate (mg/(g·min)). **β** is the constant of desorption (g/mg).
(7)	the intraparticle diffusion	$Qt = K_{id}\,t^{0.5} + C$	**k_{id}** (mg.g^{-1} $min^{-0.5}$) is the rate constant of intraparticle diffusion. **C** is the intercept.
(8)	Fractional power	$lnQ_t = \ln K + \vartheta \ln t$	ϑ is the fractional power kinetic model constant. K is the fractional power kinetic model constant (mg g^{-1} h^{-1}).

2.7. Equilibrium modeling classical and advanced adsorption models

Adsorption isotherms are pivotal in understanding the interactions between adsorbates and adsorbents, serving as indispensable tools for optimizing adsorbent utilization and providing crucial insights into determining adsorbent capacity. In our investigation, we acknowledge the significance of concentration gradients in propelling the adsorption process. Elevated concentration gradients enhance adsorption effectiveness by intensifying the driving force and facilitating mass transfer. This leads to more frequent collisions and quicker diffusion of MB molecules onto the surface of the adsorbent. However, it's important to note that high concentrations of MB may saturate adsorption sites and increase competition among molecules, consequently decreasing adsorption efficiency. Understanding these dynamics comprehensively is essential for maximizing the efficiency of adsorption systems and effectively addressing challenges posed by high dye concentrations in wastewater treatment. Our study offers crucial insights into enhancing adsorption mechanisms for efficient water filtration.

The adsorption isotherm experiments were carried out by contacting MB solutions at various concentrations (ranging from 50 to 800 mg/L) with 0.015 g adsorbent. These mixtures were stirred continuously at 250 rpm for 2 hours at three distinct temperatures (10, 20, and 30 °C). After reaching equilibrium, the solutions were separated, analyzed, and the adsorbed quantities were calculated using Eq (1).

Traditional isotherms data analysis, specifically the Langmuir, Freundlich, and Sips models, since the experimental data were fitted using three widely used conventional adsorption isotherm models. **Table 2** provides these models' fundamental formulations [40,44–47].

Table.2. shows the equations and parameters of such models.

Equation number	**Equation name**	**Equation formed**	**Parameters**

			Q_e (mg g^{-1}) is the amount of MB adsorbed per unit mass of adsorbent.
(9)	Langmuir	$\frac{Q_e}{Q_m} = \frac{K_L C_e}{1 + K_L C_e}$	**Q_m** (mg.g^{-1}) is the monolayer capacity of the adsorbent. **C_e** (mg.L^{-1}) is the equilibrium dye concentration in the solution. **K_L** the Langmuir constant.
(10)	Freundlich	$Q_e = K_F C_e^{1/n}$	**K_F** and **n^{-1}** are empirical constants indicative of sorption capacity and sorption intensity, respectively.
(11)	Sips	$\frac{Q_e}{Q_m} = \frac{(K_S C_e)^m}{1 + (K_S C_e)^m}$	**K_s** is (L mg^{-1}) the Sips constant **m** the exponent of the Sips model

278

279 Additionally, we evaluated the interactions between the examined dye, namely Methylene Blue
280 (MB), and the GP composite. This assessment involved the application of monolayer with
281 single energy (M1), monolayer with double energy (M2), and multilayer (M3) adsorption
282 models. In the context of these advanced statistical models, the subsequent calculations were
283 employed:

284 **Table.3.** The Advanced statistical physics models M1, M2 and M3 [48,49].

model	**Equation**	**Parameters**
Single-energy single-layer model eq(12)	$\mathbf{Q = \frac{Q_0}{1 + \left(\frac{C_{1/2}}{C_e}\right)^n} = \frac{n.N_m}{1 + \left(\frac{C_{1/2}}{C_e}\right)^n}}$	Q (mg.g^{-1}): adsorbed quantity. n : number of ions per site. N_m (mg.g^{-1}) : sites receptor density. Q_0 (mg.g^{-1}); adsorbed quantity at saturation
Double-energy single-layer model eq(13)	$\mathbf{Q = n.N_m.\frac{\left(\frac{C_e}{C_{1/2}}\right)^n + 2.\left(\frac{C_e}{C_{1/2}}\right)^{2n}}{1 + \left(\frac{C_e}{C_{1/2}1}\right)^n + \left(\frac{C_e}{C_{1/2}}\right)^{2n}}}$	
Multilayer model eq (14)	$\mathbf{Q = n.N_m.\frac{F_1(C_e) + F_2(C_e) + F_3(C_e) + F_4(C_e)}{G(C_e)}}$ **with**	$C_{1/2}$(mg .L^{-1}) : the concentration at half–saturation C_1 and C_2 (mg.L^{-1}) : concentrations at half saturation for the first and the second active sites respectively.

$$F_1(C_e) = \frac{\left(-2.\left(\frac{C_e}{C_1}\right)^{2n}\right)}{\left(1-\left(\frac{C_e}{C_1}\right)^{n}\right)} + \frac{\left(\frac{C_e}{C_1}\right)^{n}\left(1-\left(\frac{C_e}{C_1}\right)^{2n}\right)}{\left(1-\left(\frac{C_e}{C_1}\right)^{n}\right)^{2}}$$

$$F_2(C_e) = \frac{2.\left(\frac{C_e}{C_1}\right)^{n}\left(\frac{C_e}{C_2}\right)^{n}\left(1-\left(\frac{C_e}{C_2}\right)^{(nN_2)}\right)}{\left(1-\left(\frac{C_e}{C_2}\right)^{n}\right)}$$

$$F_3(C_e) = \frac{-\left(\frac{C_e}{C_1}\right)^{n}\left(\frac{C_e}{C_2}\right)^{n}\left(\frac{C_e}{C_2}\right)^{(nN_2)} N_2}{\left(1-\left(\frac{C_e}{C_2}\right)^{n}\right)}$$

$$G(C) = \frac{\left(1-\left(\frac{C_e}{C_1}\right)^{(2n)}\right)}{\left(1-\left(\frac{C_e}{C_1}\right)^{n}\right)} + \frac{\left(\frac{C_e}{C_1}\right)^{n}\left(\frac{C_e}{C_2}\right)^{n}\left(1-\left(\frac{C_e}{C_2}\right)^{(nN_2)}\right)}{\left(1-\left(\frac{C_e}{C_2}\right)^{n}\right)}$$

n_1 and n_2 : number of ions per site for the first and the second sites receptor respectively.

2.8. Precision of the kinetic model and adsorption isotherm

Nonlinear regression was carried out to identify the model parameters from experimental data. In nonlinear regression, the model parameters are identified to minimize the sum of squared model prediction errors.

In addition to the coefficient of determination (R^2), the normalized standard deviation ΔQ(%)defined in Eq(15) is also used to assess model performance[50].

$$\Delta Q(\%) = 100 \times \sqrt{\frac{\sum\left(\frac{Qt_{exp}-Qt_{cal}}{Qt_{exp}}\right)^2}{n-1}} \quad \textbf{(15)}$$

Where the $Qt_{,exp}$ and $Qt_{,cal}$ refer to the experimental and calculated values from kinetic adsorption and n is the number of data points.

The validity of the adsorption isotherm was also measured using the hybrid error function (HYBRID), which is defined as [51]:

$$HYBRID = \frac{100}{N-p}\sum_{i=1}^{N}\left[\frac{(Q_{t,exp}-Q_{t,cal})^2}{Q_{exp}}\right] \quad \textbf{(16)}$$

Where $Q_{t,exp}$ is the observation from the batch experimental, $Q_{t,\,cal}$ is the estimate from the isotherm for corresponding Q_{exp} , N is the number of observations in the experimental isotherm and p is the number of parameters in the regression model.

2.9. The thermodynamic study

The energy changes that take place during an adsorption process can be seen by using thermodynamic parameters like Gibbs free (ΔG°), enthalpy (ΔH°), and entropy (ΔS°), which can also be used to investigate the impact of temperature. The following equations are used to compute these parameters [52] :

$$K = \frac{\mathbf{1000}*Qe}{Ce} \quad \textbf{(17)}$$

$$\Delta G = -RT\ln K \quad \textbf{(18)}$$

$$\Delta G = \Delta H - \Delta S \quad \textbf{(19)}$$

In the above equations, K is the equilibrium constant; T (K) is the adsorption temperature; R (8.314 $J{\cdot}mol^{-1}{\cdot}K^{-1}$) is the universal gas constant. The ratio 'Qe/Ce' acts as the Langmuir equilibrium constant at various temperatures. In general, ΔH° and ΔS° are calculated from the slope and intercept of ΔG° versus T.

2.10. Specifics of the Density Function Theory

The characterization of the systems under investigation is substantially contingent on the frontier molecular orbitals (FMOs), specifically the Highest Occupied Molecular Orbital (HOMO) and the Lowest Unoccupied Molecular Orbital (LUMO), which are determined

utilizing the Density Functional Theory (DFT) with the DMOl3 technique. The energies associated with HOMO and LUMO play a pivotal role in quantum chemical computations, as they furnish crucial insights into the microscopic interactions occurring within adsorption systems. These parameters are integral to quantum chemistry simulations, and the computed energy values for E_{HOMO}, E_{LUMO}, and E_o are presented in the formulae below [53].

The following formulas are employed to determine potential (μ), electronegativity (χ), global hardness (η), global softness (S), global electrophilicity index (ω), softness (σ), and the maximum amount of electronic charge (ΔN_{max}).

$$\mu = E_{HOMO} + E_{LUMO} \quad \textbf{(20)}$$

$$\mathcal{X} = -\mu \quad \textbf{(21)}$$

$$\eta = \frac{E_{LIMO} - E_{HOMO}}{2} \quad \textbf{(22)}$$

$$S = \frac{1}{2\eta} \quad \textbf{(23)}$$

$$\omega = \frac{\chi^2}{2\eta} \quad \textbf{(24)}$$

$$\sigma = \frac{1}{\eta} \quad \textbf{(25)}$$

$$\Delta N_{max} = \frac{-\mu}{\eta} \quad \textbf{(26)}$$

2.11. Description of Molecular Dynamic Simulation

All molecular dynamic simulations (MDS) conducted in this study were executed utilizing the BIOVIA MATERIALS STUDIO 2020 software. In these simulations, the GP (-1 0 0) surface was employed as the substrate for investigating the adsorption of MB onto the GP surface. The application of periodic boundary conditions defined a simulation box with dimensions of (27 Å × 27 Å × 15 Å), encompassing the GP slab, the MB molecule, and a vacuum slab. Geometrical

refinement of the MB molecular structure and the GP (-1 0 0) surface was achieved by energy minimization. Employing a time step of 0.1 femtoseconds (fs) and a simulation duration of 50 picoseconds (ps), the COMPASS force field model was applied under the NVT ensemble during the course of the molecular dynamic simulations.

2.12. Regenerative Characteristics

In the desorption process, electron transfer between MB dye and the ethanol solvent is essential for releasing MB molecules from the adsorption sites on the biosorbent. Effective electron transport, facilitated by suitable electron sources or acceptors present in the system, promotes increased desorption kinetics. This process can occur through redox reactions, where electron donors donate electrons to the MB dye, aiding its detachment from the biosorbent surface, or where electron acceptors take electrons from the MB dye, facilitating its release into the solvent. Desorption experiments were conducted using a 0.1 M ethanol solution. Following each adsorption cycle, the adsorbent material was immersed in 50 mL of 0.1 M ethanol solution for 1 hour and then dried at 60°C for 30 minutes. Post-adsorption, the concentration of MB in the solution was measured to compute removal efficiency and adsorption capacity. The addition of adequate electron donors or acceptors in the ethanol solution significantly enhances desorption efficiency, resulting in more efficient removal of MB from the biosorbent material.

2.13. Gaussian Process Regression coupled with Lévy flight distribution

The seamless integration of Gaussian Process Regression (GPR) with the Lévy flight distribution constitutes a refined statistical modeling approach aimed at delving deeply into the intricate structure and inherent variability of the data. GPR, rooted in Gaussian stochastic processes, operates under the assumption that observations stem from a multivariate normal distribution *[54,55]*, thereby establishing connections between each data point through a covariance matrix *[56]*. This methodology adeptly captures both the general trend in the data

and the uncertainty associated with each prediction, proving particularly relevant in contexts where relationships between variables are as diverse as they are nonlinear *[30]*. Key features of GPR encompass the specification of covariance, often defined by a kernel, which articulates the similarity between different observations *[55]*. The model is then meticulously adjusted to maximize the likelihood of observed data while incorporating regularization to forestall any undesirable overfitting *[55]*.

Simultaneously, the Lévy flight distribution distinguishes itself with large amplitude jumps between states, offering a dynamic alternative to the standard random walk traditionally constrained in its jumps *[57]*. This characteristic is crucial for modeling rare events or phenomena likely to exert significant impacts on the data, introducing an additional dimension of robustness to the model *[57]*. Key aspects of the Lévy flight distribution include the meticulous determination of the stability parameter, precisely governing the probability of large amplitude jumps *[57]*. A higher stability index promotes more frequent and larger jumps, reinforcing the model's ability to respond to data intricacies *[57]*.

The synergistic union between Gaussian Process Regression and the Lévy flight distribution aims to optimally leverage the intrinsic advantages of these two distinct approaches. The resulting model capitalizes on the flexibility of GPR to model the underlying structure of the data while integrating the unique capability of the Lévy flight distribution to capture rare events and significant jumps. GPR ensures the provision of a comprehensive prediction enveloped in confidence intervals, while the Lévy flight distribution introduces an unprecedented dimension to finely capture unpredictable phenomena. The model adjustment process involves a meticulous estimation of the parameters of the GPR kernel and the stability parameter of the Lévy flight distribution, a crucial step to optimize model performance while guarding against overfitting risks. Thus, this holistic approach provides a comprehensive solution for modeling complex data, combining the agility of GPR to provide probabilistic predictions with the

distinctive power of the Lévy flight distribution to represent rare events and abrupt changes, shaping a statistical modeling tool of great finesse.

Within this research endeavor, the integration of GPR with LFD, denoted as GPR_LFD, has been utilized as a pivotal and sophisticated method for predicting the adsorbed quantities of MB by GP. Utilizing parameters meticulously optimized in the preceding section, the predictive model encompasses a comprehensive set of influential variables, including contact time (X1), adsorbent mass (X2), MB concentration (X3), pH (X4), and Temperature (X5). After the establishment of the database, a normalization process was applied to confine its values within the interval [-1,1]. Subsequently, the dataset underwent a meticulous division, allocating 70% for training, 15% for validation, and the remaining 15% for stringent testing to rigorously assess the efficiency and generalization capability of the finest model.

During the intricate model creation phase, a thorough exploration and optimization process encompassed ten distinctive kernel functions. This exhaustive set included, among others, exponential, exponential squared, Matern32, Matern52, quadratic rational, ARD exponential, ARD exponential squared, ARD Matern32, ARD Matern52, and ARD quadratic rational. The optimization process was nuanced, involving the exploration of various basis functions such as constant, linear, PureQuadratic, and zero, while simultaneously fine-tuning the parameters (Kernel Scale [sigmaM, sigmaF], and sigma) for each kernel function.

In this study, we present a novel contribution by introducing and implementing the GPR_LFD approach, marking the first application of this innovative amalgamation of the Lévy Flight Distribution algorithm with Gaussian Process Regression in adsorption. This distinctive combination sets our research apart from earlier proposals and opens new avenues for exploration in adsorption. It signifies a significant leap forward in the optimization of hyperparameters for machine learning algorithms. This approach promises not only enhanced

411 results but also improved adaptability across diverse applications and datasets, underscoring its
412 potential as a robust and versatile modeling tool.

413 The integration of Lévy Flight Distribution (LFD) optimization and Gaussian Process
414 Regression (GPR) prediction within MATLAB culminates in a sophisticated framework that
415 yields multifaceted advantages across diverse domains *[58]*. Foremost, this amalgamation
416 engenders heightened optimization prowess by synergizing the exploratory efficiency of LFD
417 with the predictive accuracy of GPR *[58]*. By traversing the search space adeptly, LFD
418 optimally navigates complex landscapes, while GPR adeptly synthesizes insights from limited
419 data, culminating in refined optimization outcomes surpassing those achievable through
420 singular methodologies *[58]*.

421 Moreover, the fusion of LFD and GPR manifests in the manifestation of robust predictive
422 models. GPR's capacity for discerning underlying patterns from sparse datasets harmonizes
423 seamlessly with LFD's ability to expedite model training and parameter refinement *[58]*. This
424 symbiosis empowers the construction of predictive models endowed with unparalleled accuracy
425 and adaptability, capable of elucidating system behaviors across varying contexts with
426 remarkable fidelity *[58]*.

427 A salient consequence of this integration is the judicious allocation of resources. By leveraging
428 MATLAB's computational prowess, this amalgamated approach optimizes resource utilization,
429 mitigating time, computational, and experimental expenditures. Such efficiency not only
430 expedites decision-making processes but also augments cost-effectiveness, thereby fortifying
431 its appeal across sectors characterized by resource constraints *[58]*.

432 Furthermore, the versatility of this integrated framework is unequivocal. Its applicability spans
433 myriad domains, from engineering and finance to healthcare and environmental science. Such
434 universality underscores its status as a potent toolset capable of addressing optimization and

prediction imperatives in multifarious contexts, thereby facilitating paradigm shifts and catalyzing innovation across diverse disciplines.

In conclusion, the integration of LFD optimization and GPR prediction using MATLAB represents a pinnacle in computational methodology, heralding a new era of optimization efficacy, predictive precision, resource efficiency, and cross-disciplinary applicability. As the frontier of computational science continues to evolve, this integrated framework stands as a beacon of innovation, promising to illuminate pathways to transformative advancements across the spectrum of human endeavor.

2.13.1. **Statistical evaluation criteria**

In the present study, the performance of each GPR model was evaluated using various model performance measures including the Correlation Coefficient (R) and Root Mean Squared Error (RMSE) *[59–65]*:

$$R = \frac{\sum_{i-1}^{N}(y_{exp}-\bar{y}_{exp})(y_{pred}-\bar{y}_{pred})}{\sqrt{\sum_{i-1}^{N}(y_{exp}-\bar{y}_{exp})^2 \sum_{i-1}^{N}(y_{pred}-\bar{y}_{pred})^2}} \quad \textbf{(27)}$$

$$RMSE = \sqrt{(\frac{1}{N})(\sum_{i-1}^{N}(y_{exp} - y_{pred})^2} \quad \textbf{(28)}$$

Where N is the number of data samples; y_{exp} and y_{pred} are the experimental and the predicted values respectively; $\bar{y}_{exp}$ and $\bar{y}_{pred}$ are respectively the average values of the experimental and the predicted values [66–70].

3. Results and discussion

3.1. Characterizations

Figure S2 illustrates the diffraction pattern of GP, manifesting a distinct prominent peak at 2θ = 22° attributed to the (0 0 2) crystallographic plane, alongside a minor peak at 2θ = 15° corresponding to the (1 0 1) plane [44,71]. The XRD spectrum shows that for the 2 theta analysis

range above 40°, there are no distinct diffraction peaks of crystalline cellulose. Instead, there are mainly amorphous peaks. This implies that the predominant components of the native pulp are non-cellulosic substances, such as hemicellulose and lignin [44,71]. These observations collectively signify the characteristic structural features associated with cellulose I.

FT-IR characterization was employed to quantitatively appraise the functional categories that are identifiable on the pure green peel (GP) samples. Both acid-activated (OP-H_3PO_4) and alkali-activated (OP-KOH) samples were analyzed for comparative purposes. The outcomes, as depicted in **Figure 1**, reveal the presence of distinct absorption bands. Notably, the surface of GP exhibited a higher concentration of alcoholic and phenolic -OH functional groups in comparison to cellulose, as evidenced by a broad absorption band at 3341 cm^{-1} [72]. Additional spectral features included weak bands at 2924 cm^{-1}, indicative of hydrophobic CH_2 asymmetrical and symmetrical stretching vibrations, and a band at 1623 cm^{-1}, corresponding to C=O and N-H functionalities, potentially associated with amide I groups [73]. Furthermore, the band at 1320 cm^{-1} was attributed to the C-H group, and at 1030 cm^{-1}, stretching vibrations corresponding to O-H and C-OH were identified, indicative of the presence of polysaccharides within cell walls, such as arabinan and cellulose [74].

Figure 2 indicates that the pHpzc (point of zero charge) of the adsorbent was determined to be 5.5. This implies that the GP surface exhibited a positive charge when the solution's pH was lower than 5.5 and a negative charge when the solution's pH exceeded 5.5.

Within this pH range, MB is found in both cationic (tri-protonated, or MBH_2^+) and undissociated (MB°) forms. The cationic forms mono-protonated (MBH) and di-protonated (MBH_2^+) occur for pH values higher than 6, with the latter form species predominating [75]. However, with pKa values greater than 8.33, the nitrogen atom in the MB molecule's core cycle is completely deprotonated, leaving the MB dye negatively charged (MB-). Because our biomaterial has a negative charge as a result (pH>5.5), we chose the cationic dye (MB).

Figure 3 depicts the scanning electron microscope (SEM) analysis of the surface morphology of GP biomass during the adsorption process of MB dye, conducted at varying magnifications ranging from 100 to 5 μm and at an accelerating voltage of 5 kV. Furthermore, the raw green peel exhibits a distinct structural characteristic. The SEM imagery reveals the presence of abundant pores and an irregular surface structure within the fibers of the GP [76]. It is clearly illustrated that the enhanced adsorption potential can be attributed to this specific surface feature of the fiber material.

The BET characterization of Green Peel (GP) shows a surface area of 85.672 m^2/g, indicating a substantial amount of available surface for adsorption. This high surface area suggests that GP has significant potential for adsorbing Methylene Blue (MB) or other substances, reflecting its effectiveness as an adsorbent. The result points to GP's promising performance in adsorption applications, although further analysis of its pore structure and adsorption dynamics would provide additional insights.

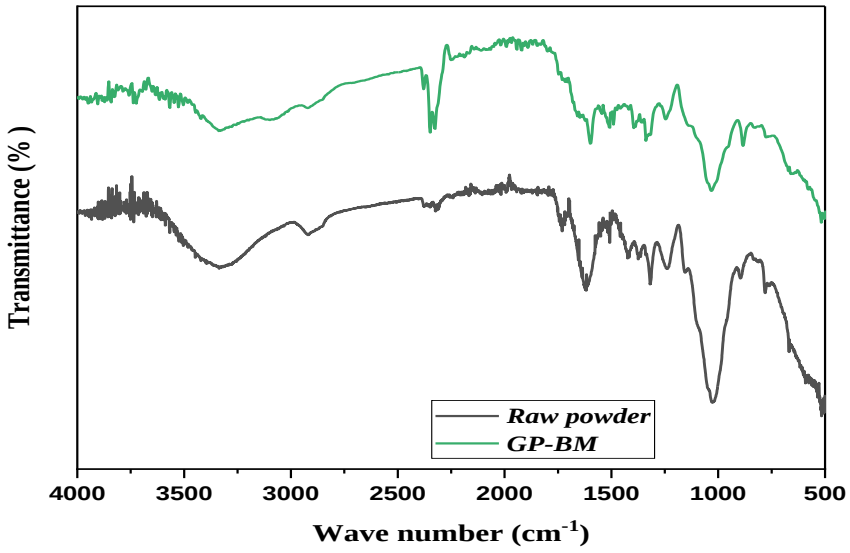

Figure.1. FTIR characterization of biomass (raw and GP-BM).

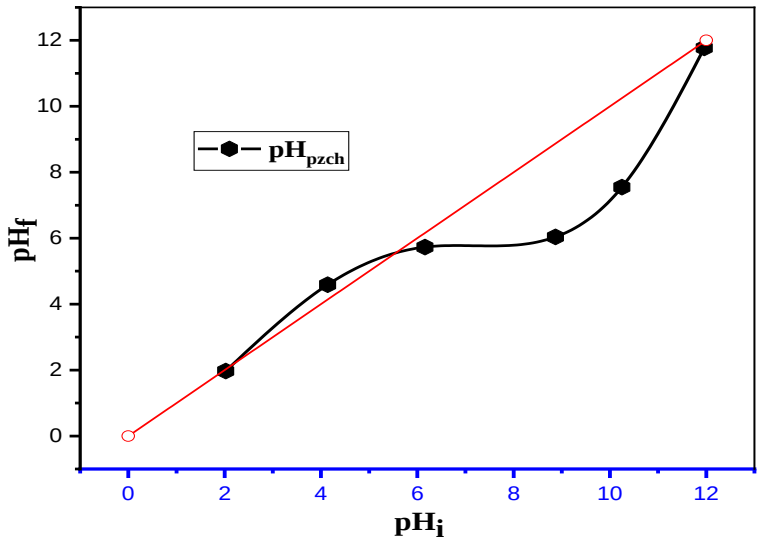

497

498 **Figure.2.** Determination of the zero charge point of GP raw.

499

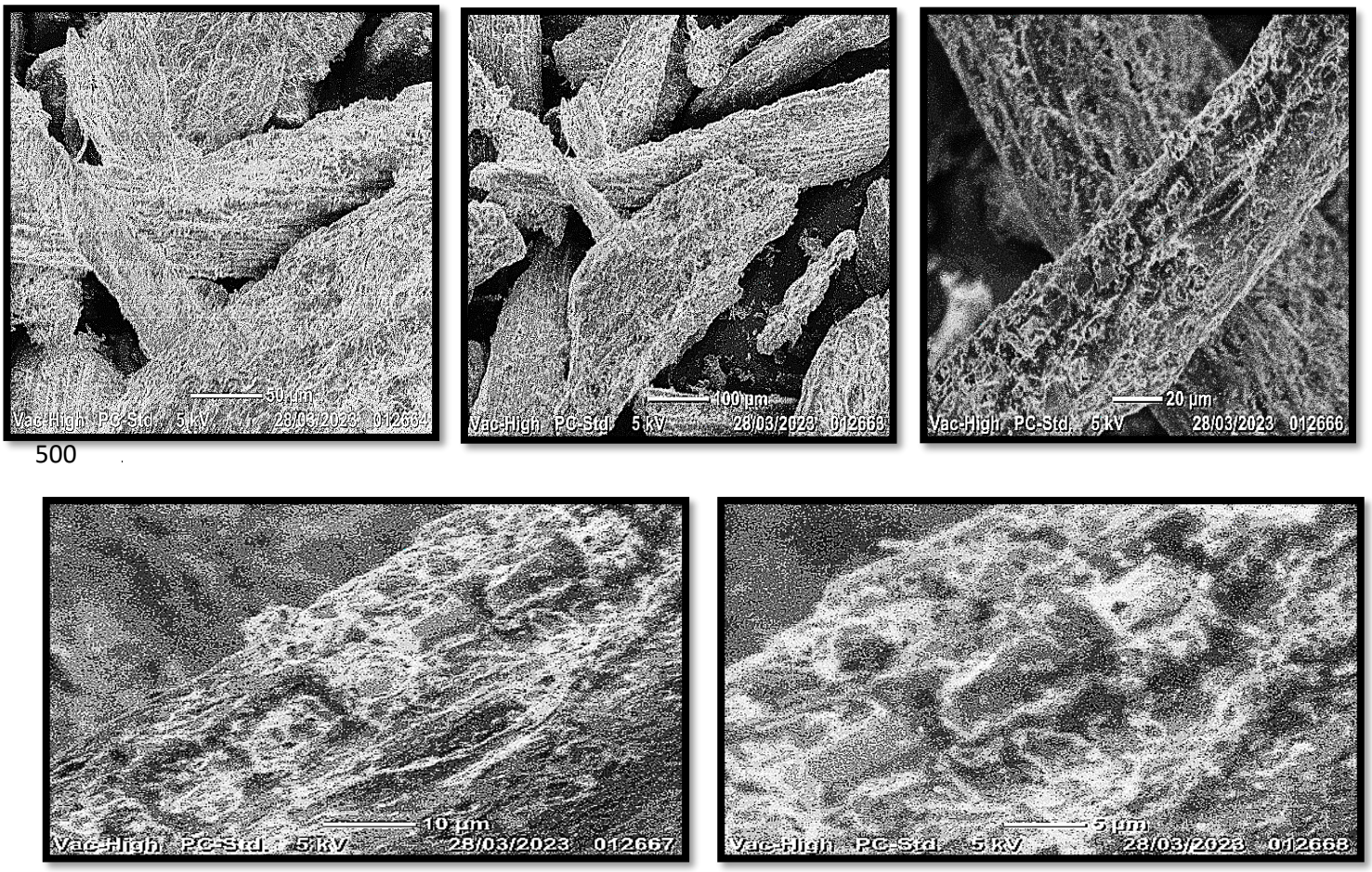

500

501 **Figure.3.** SEM images of a GP raw.

502 **3.2. Effect of adsorbent dose**

Figure 4 illustrates the impact of the mass of adsorbent on the binding of MB. It reveals a reduction in the adsorption capacity per unit mass of adsorbent as the adsorbent mass increases. This reduction is accompanied by an increase in the absorption rate, leading to enhanced pollutant removal. This phenomenon may be attributed to an increase in the available surface area and the number of active sites on the surface of GP material[26].

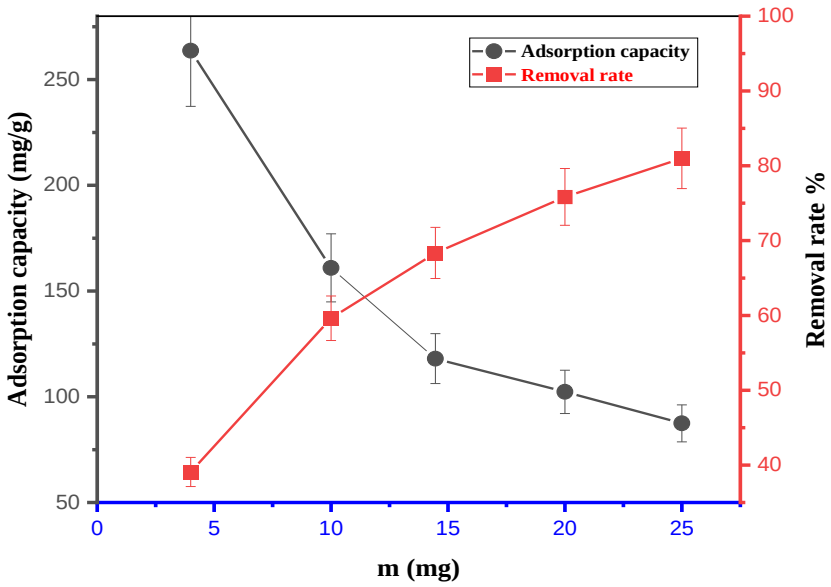

Figure.4. Effect of adsorbent dose on the adsorption of MB on GP (C_o: 100 mg. L^{-1}, Contact time: 30 min).

3.3. Effect of pH

Figure 5 indicates how the pH of an aqueous solution affects the MB adsorption on GP material. The findings illustrate that under acidic conditions (pH < 6), the adsorption capacity of (GP) exhibits an augmentation from 10.6 to 111.22 mg/g. Conversely, under alkaline conditions (pH > 6), there is a reduction in adsorption capacity to 107.56 mg/g. At very low starting pH levels, there is relatively little MB absorption. This is brought on by the protonation of the adsorbate (MB) in an acidic environment and the competition with excess H^+ ions and dye cations for active sites. Because of electrostatic attraction, there are fewer strongly charged sites and more less charged sites when the pH of the solution rises. The negatively charged adsorbent surface

at greater pH values changes the polarity of the adsorbent by forming an electric double layer, resulting in dye adsorption [77].

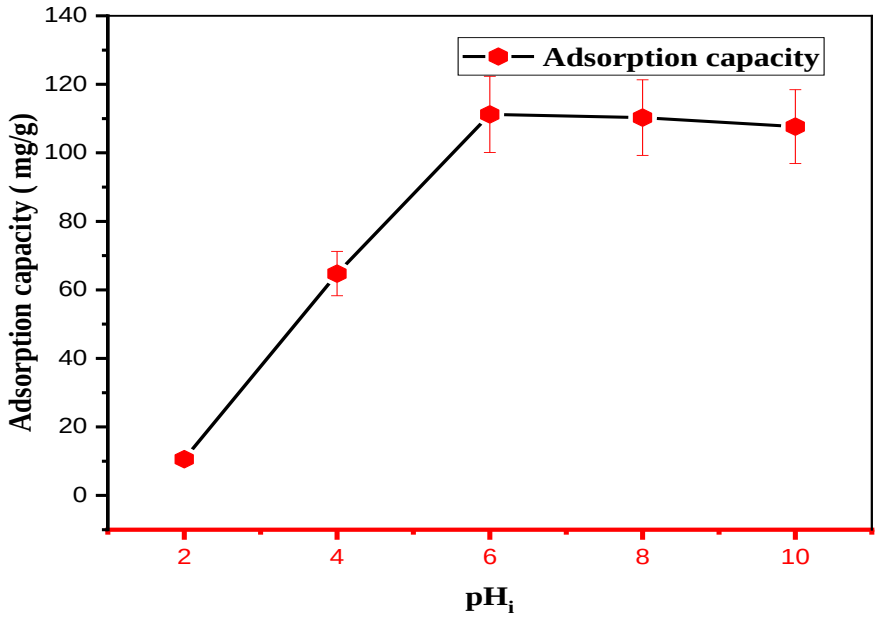

Figure.5. Influence of pH on the adsorption of BM on GP (m_{GPb}: 0.015 g, C_o: 0.1 g/L, Contact time: 30 min).

3.4. Removal Kinetics in Relation to Contact Duration

In **Figure S3**, the impact of contact duration on the adsorption capability of the biosorbent under investigation is depicted for dye concentrations ranging from 50 to 250 mg/L. The dye solution was allowed to come into contact with the biosorbents for 24 hours in order to calculate the adsorption capacity at equilibrium, Qe_{exp}, **(Table 1)**. However, the data points shown in **Figure S3** are only for the first 30 minutes because there were no noticeable changes in the adsorption capacity of the biosorbent under study after that point. Due to the presence of multiple functional groups on the surface of all biosorbents during the first stages of adsorption, which led to highly attractive interactions between dye molecules and adsorbent, the adsorption capacity of MB dye rose fast in the first 15 min. The concentration of adsorbed dye grew slowly during prolonged contact durations, converging after 30 minutes to a value close to equilibrium.

The outcomes of the nonlinear regression of the PFO, PSO, and PNO equations are shown in **Figure 6**. **Table 4** summarizes the parameters they were able to gather. At the beginning and for the first five concentrations (50, 100, 150, 200, and 250 mg L^{-1}), respectively. The PFO-derived curves are flatter than the experimental data from adsorption. They surpass the experimental results for the latter step of adsorption, on the other hand. Given a little variation in the beginning stage time, the same observation for the PSO-derived curves. Because of this, there is another order n besides 1 and 2 that offers the least amount of variation throughout the adsorption process [78]. The Elovich model's poor R^2 values **(Table 4)** showed that pore diffusion was not the primary factor influencing MB adsorption onto GP.

The PNO-derived curves that deviate the least from the experimental data support this assertion, and all of this was supported by **Table 4** normalized standard deviation (ΔQ%) and the correlation coefficient R^2 values. The correlation coefficients of the pseudo-nth-order kinetic model exhibit strong correlation coefficients and low average percentage error values. This model performs better than the pseudo-first and pseudo-second-order equations and matches the experimental data nicely. For concentrations of 50, 100, 150, 200, and 250 mg L^{-1}, the order of the adsorption reaction n was discovered to be between 1.09, 1.41, 5.14, 1.26, and 2.98, respectively.

The rate-controlling step is intraparticle diffusion, and the plot of (qt) vs ($t^{1/2}$) should be linear and pass through the origin. The correlation coefficients in this study ($0.978 < R^2 < 0.989$) show that the adsorption closely resembles the intra-particle diffusion model. However, the intercept does not pass through the origin, indicating that intra-particle diffusion is not the rate-limiting step. This shows that there are three unique zones, with the first being curved, the second being linear, and the third being horizontal lines. The first area is swift and is a result of the outward diffusion of MB molecules from their exterior surface. The diffusion of MB molecules in the pores is regulated by intra-particle diffusion (inner diffusion) during the progressive adsorption

stage, which causes the second area. The intraparticle diffusion is beginning to slow down in the third area, which is the last equilibrium stage, as a result of the low concentration of MB in the solution. Further observations show that the boundary layer thickens as Co is increased from 50 to 250 mg L^{-1}, which is explained by a decrease in the likelihood of external mass transfer and an increase in the likelihood of internal mass transfer.

Additionally, it was discovered that the intra-particle-diffusion rate constant, k_p, increased as the initial MB concentration increased, indicating that the boundary layer may have played a role in the growing driving force for the mass transfer between the solution and GP surface [79]. As shown by the positive and less than 1 value of v in the fractional power model, this model should explain the mechanism. However, the poor values of the correlation coefficient (R^2) along with the capacity calculated using this model are not close to the experimentally obtained value, indicating that this model is also not applicable (**Figure 6**).

Table.4. Kinetic Parameters for nonlinear regression of BM Adsorption onto GP.

models	**Parameters**	50 mg.L^{-1}	100 mg.L^{-1}	150 mg.L^{-1}	200 mg.L^{-1}	250 mg.L^{-1}
PFO	**Q_{exp}**	45.54	96.49	143.26	196.98	238.09
	Qe	50.94	97.94	133.41	146.54	156.18
	K_1	0.138	0.159	0.197	0.205	0.394
	R^2	0.989	0.988	0.948	0.994	0.990
	ΔQ%	**0.140**	**0.002**	**0.047**	**0.692**	**1.183**
PSO	**Qe**	56.68	106.46	146.10	157.50	161.95
	K_2	0.003	0.002	0.002	0.002	0.006
	R^2	0.976	0.989	0.983	0.992	0.997
	ΔQ%	**0.598**	**0.106**	**0.003**	**0.433**	**1.022**
PNO	**Qe**	51.27	100.06	202.007	148.52	170.18
	K_n	0.004	0.005	$1.09*10^{-10}$	0.007	$4.42*10^{-5}$

	n	1.09	1.41	5.14	1.26	2.98
	R^2	0.986	0.992	0.992	0.996	0.998
	ΔQ%	0.158	0.013	1.681	0.641	0.813
Elovich	**a**	65.73	264.51	585.78	2352.44	$1.751*10^7$
	B	0.114	0.058	0.052	0.058	0.112
	R^2	0.945	0.971	0.993	0.973	0.997
Intraparticule	Kp	18.845	35.504	49.532	52.137	53.097
	C	2.723	7.655	11.763	17.894	29.727
	R^2	0.914	0.932	0.959	0.899	0.838
Fictional power	**K**	3.11	3.907	4.35	4.482	4.844
	ν	0.177	0.12	0.091	0.082	0.033
	R^2	0.840	0.9	0.953	0.855	0.928

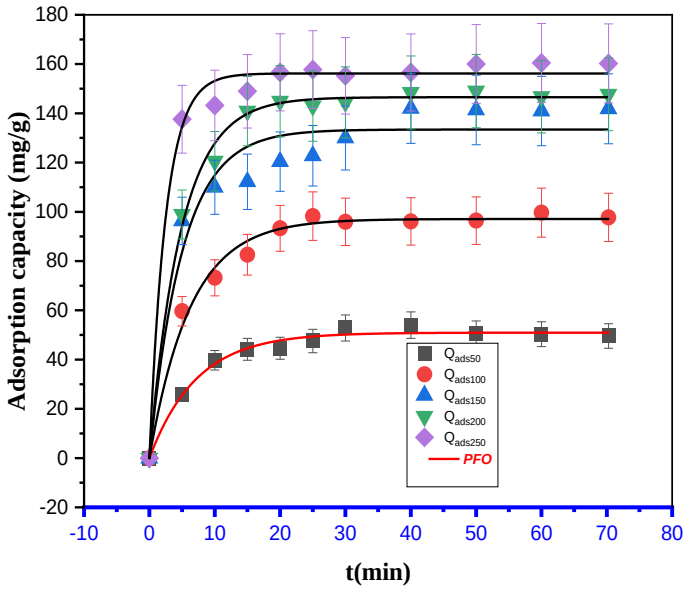

574

575 **(a)**

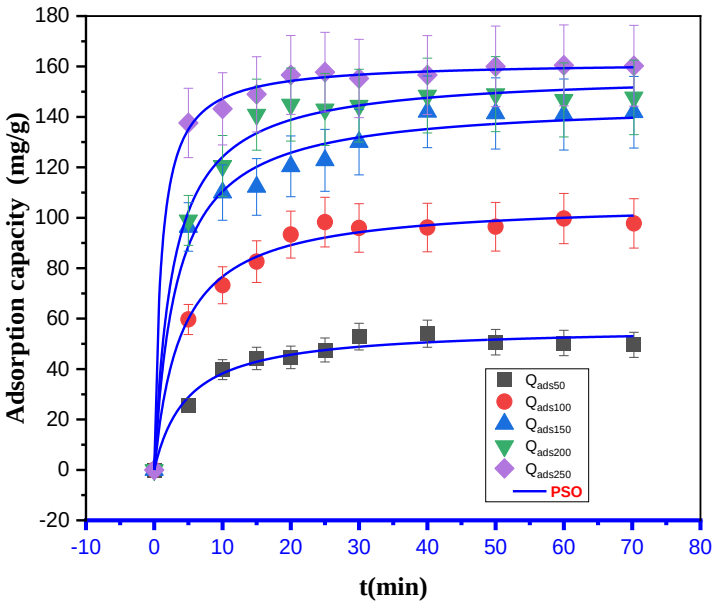

576

577 **(b)**

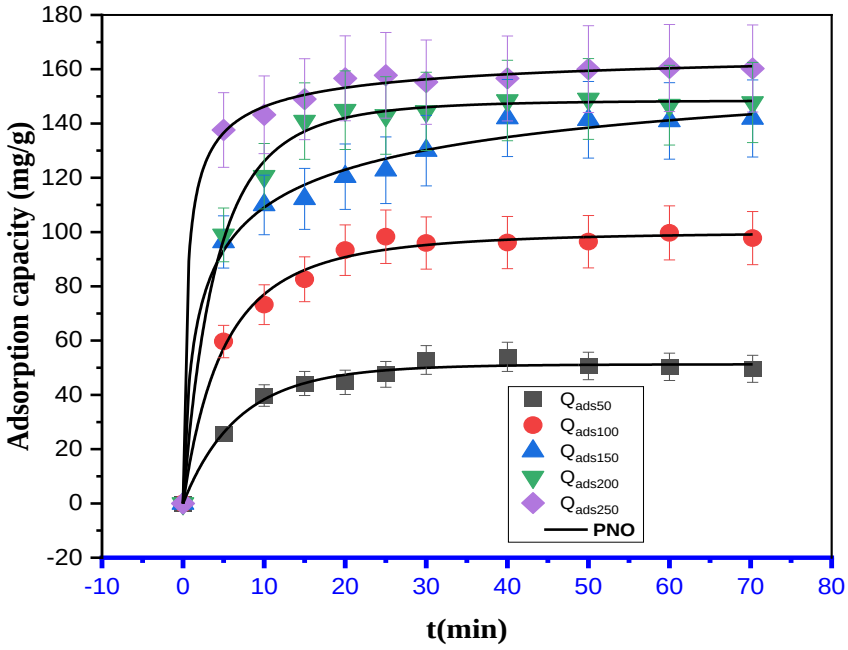

578

579 **(c)**

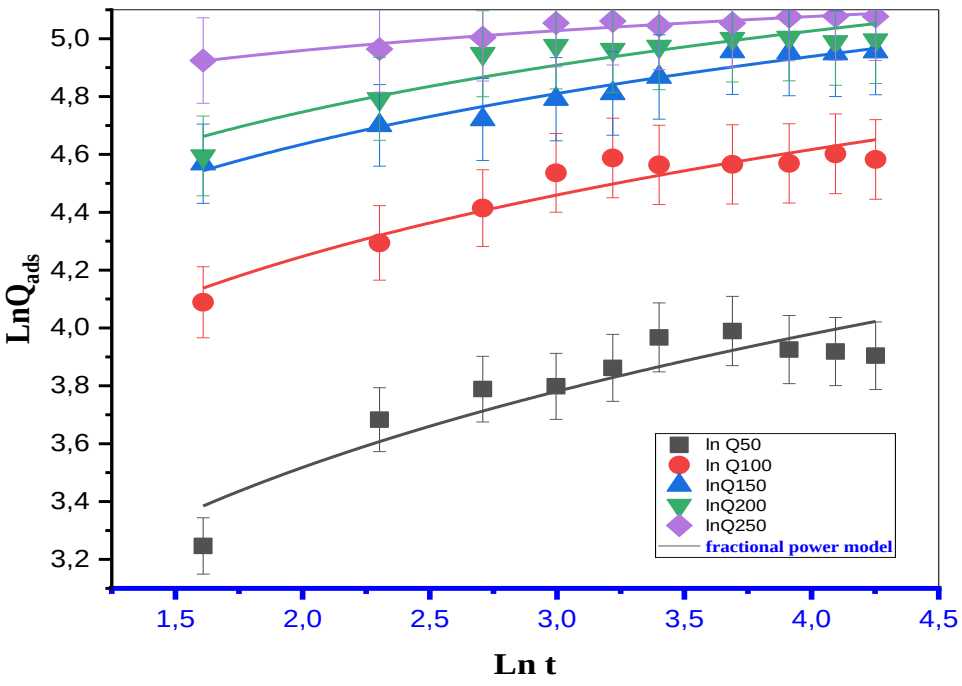

580

581 **(d)**

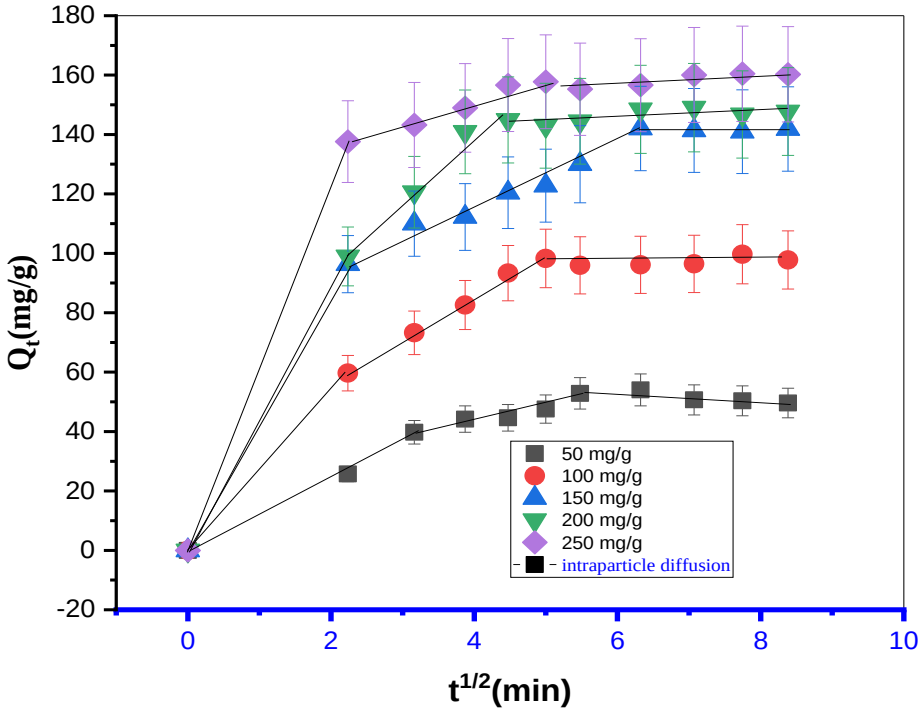

582

583 **(e)**

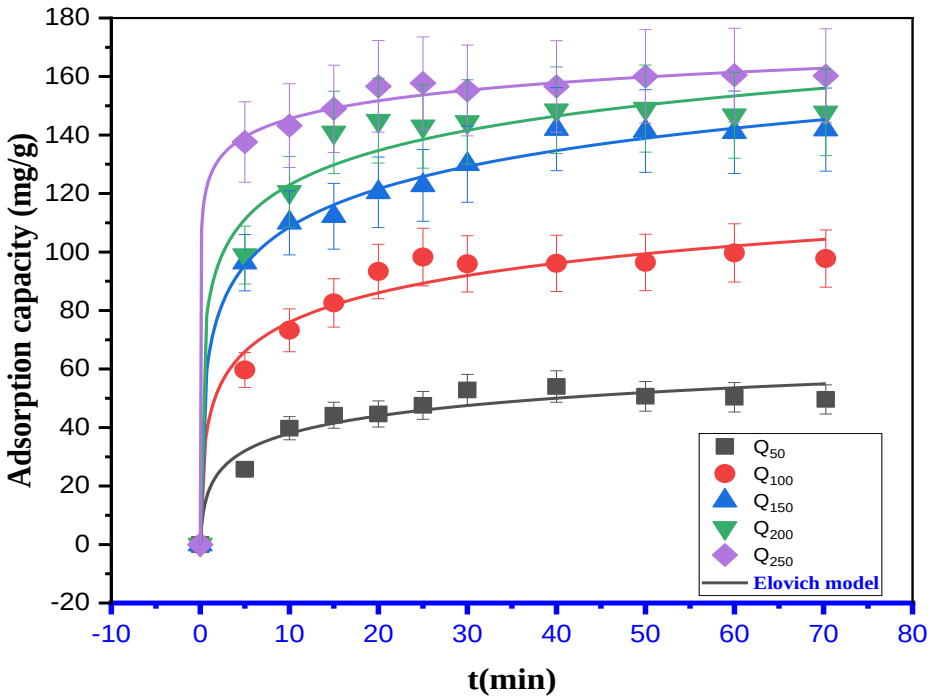

(f)

Figure.6. graph representative of Nonlinear simulation of the pseudo-first-order (a), pseudo-second-order (b), pseudo-nth-order (c), fractional power (d), intraparticle (e), and Elovich kinetic models (f). (m = 30 mg, v = 50 ml, stirring = 250 ppm, T = ambient temperature).

3.5. Adsorption isotherm study

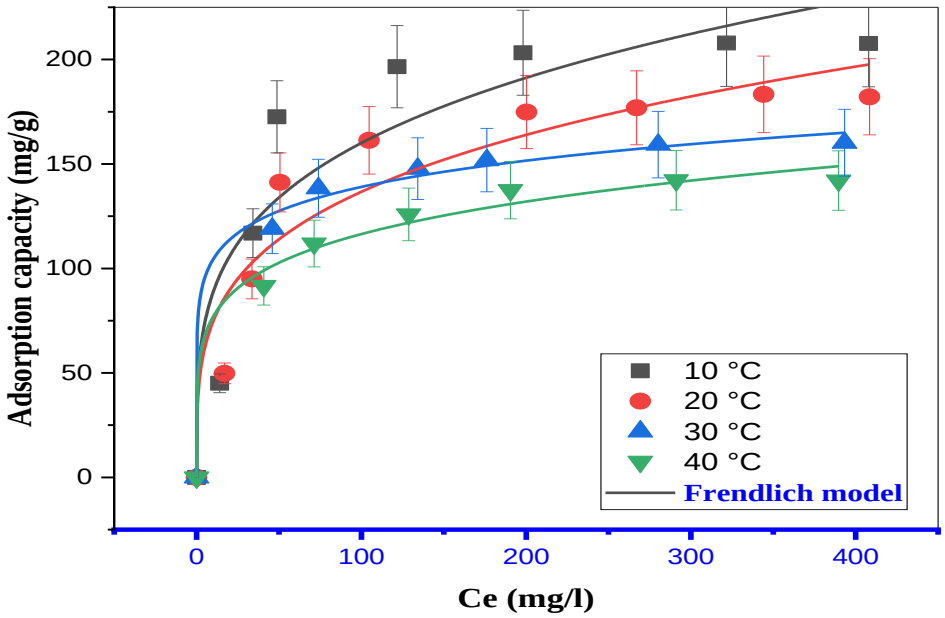
Adsorption capacity (mg/g)
200
150
100
50
0
0
100
200
300
400
Ce (mg/l)
10 °C
20 °C
30 °C
40 °C
Frendlich model

591

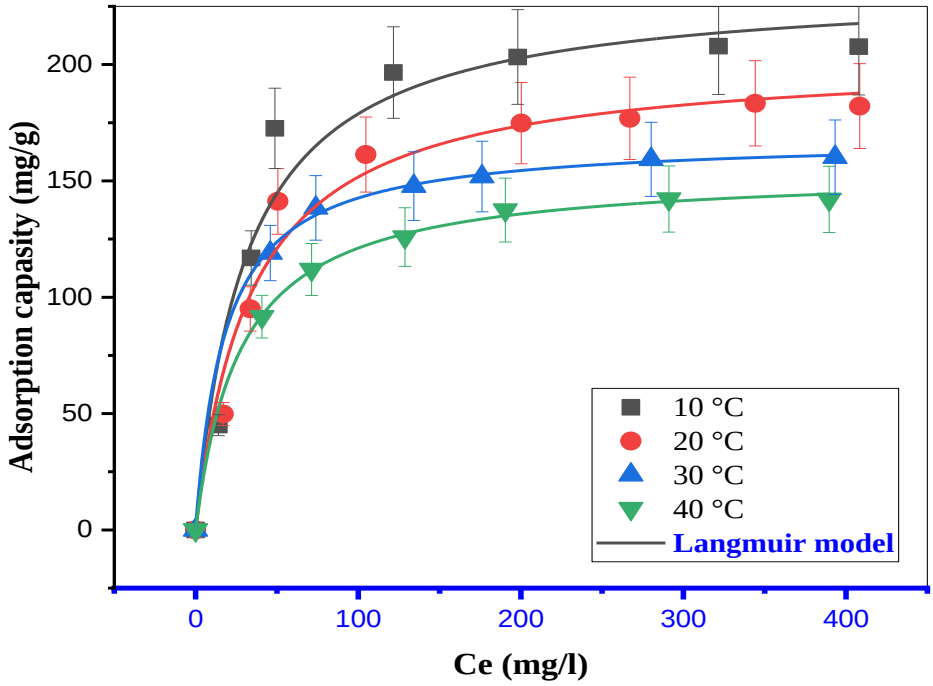
Adsorption capasity (mg/g)
200
150
100
50
0
0
100
200
300
400
Ce (mg/l)
10 °C
20 °C
30 °C
40 °C
Langmuir model

592

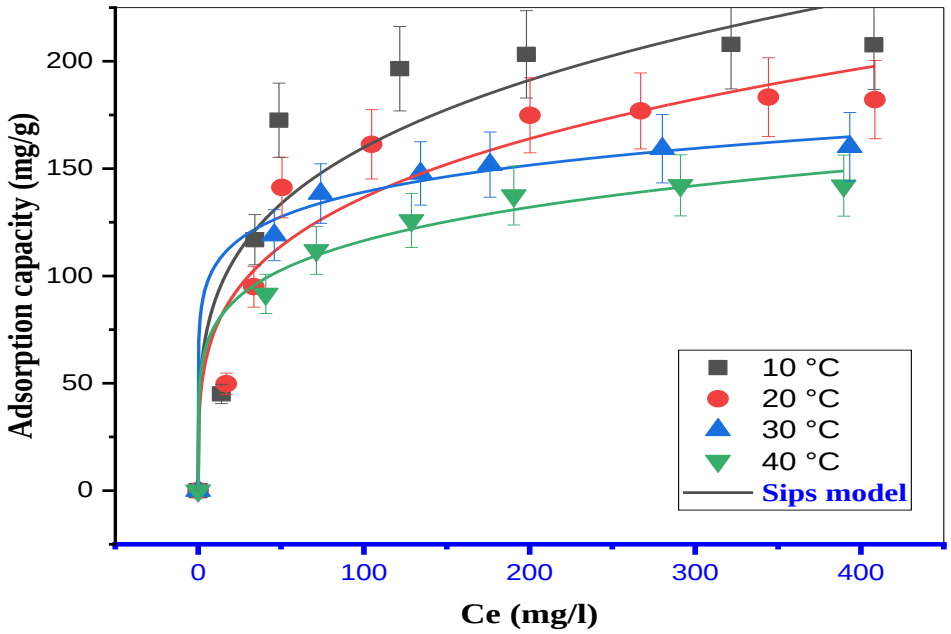

Figure.7. Result of fitting isotherms data of MB adsorption onto GP with Langmuir, Freundlich and Sips models. (m = 15 mg. v = 25 ml. stirring = 250 ppm. $pH_{natural}$).

The hybrid error function (HYBRID) and fitting parameters are displayed in **Table 5**. By contrasting the (HYBRID) and R^2 scores for data fit. The high coefficients ($R^2 > 0.99$) and the lower HYBRID levels demonstrate that the Langmuir model provides the best applicability to the equilibrium adsorption data with a monolayer of MB attributed to a homogeneous distribution of active sites on the surface of the GP. The maximum monolayer adsorption of MB on GP was observed to be 207.33 mg/g at 10 °C, decreasing to 148.52 mg/g at 40 °C. This reduction at higher temperatures is attributed to desorption, facilitated by the formation of more hydrophobic bonds between the MB molecules in water. These bonds decrease the contact between the molecules and the adsorbent surface [79], as molecules in water tend to detach from the surface to which they adhere as temperature rises. This phenomenon occurs because, with increased temperature, molecules in water exhibit a tendency to form stronger bonds with each other, thereby diminishing their affinity for the surface. A high tendency for the adsorption of the MB on the GP is indicated by values of 1/n for the Freundlich isotherm between 0 and 1, whereas lower R^2 values imply that the model is inadequate for adjusting experimental data.

The three conventional models that were utilized to build the MB uptake dynamic are inadequate. The setup and regulation of the MB-GP interaction are therefore considered as requiring the help of theoretical treatment using sophisticated models.

Table.5. Different Isotherm model parameters for the adsorption of MB onto GP.

Models	Parameters	10 °C	20 °C	30 °C	40°C
Langmuir	**Q_{exp}(mg • g^{-1})**	**203.333**	**192.187**	**179.380**	**147.828**
	Q_m(mg • g^{-1})	234.161	203.351	168.405	154.527
	K_L (L • mg^{-1})	0.032	0.029	0.055	0.036
	R^2	**0.997**	**0.997**	**0.999**	**0.999**
	HYPRID	**3.887**	**8.649**	**7.677**	**0.014**
Freundlich	N	3.890	3.813	8.006	5.526
	K_F(mg•g^{-1})(L/mg)$^{1/n}$	48.993	40.853	78.215	50.609
	R^2	**0.876**	**0.915**	**0.994**	**0.989**
	HYPRID	**19.850**	**1.055**	**11.734**	**1.066**
Sips	Q_m(mg•g^{-1})	126.71	115.05	99.60	71.41
	K_S (L•mg^{-1})	0.05276	0.09661	0.062117	1.4016
	M	1.05426	1.03999	1.1606	1.108
	R^2	**0.92913**	**0.90737**	**0.98158**	**0.91354**
	HYPRID	481.237	**516.00**	**519.374**	**658.377**

3.6. Sophisticated statistical physics models

Our trial isotherm information was subjected to simulation applying ORIGIN software (version 2018). In **Figure 8**, we determined the most suitable model or models for comprehending MB adsorption onto GP material by assessing the correlation coefficient R^2 as detailed in **Table 5**. The optimal model from advanced statistical physics for describing the MB adsorption onto the GP adsorbent was identified as the double-energy single-layer model.

3.6.1. Steric parameters

3.6.1.1 Parameter n

The adsorption geometry (vertical or horizontal) and uptake method (multi-docking or multi-interactions) of the studied dye MB on GP adsorbent may both be explained by the steric n parameter, where n is the number of dye molecules adsorbed per active site of the adsorbent

(GP). Based on the n parameter, three primary situations are often recognized when defining the adsorption shape and mechanism: Si (n > 1) MB adsorption can occur in a vertical geometry via a multi-interaction process, when (n < 1) MB adsorption takes place horizontally via a multi-docking process (multiple GP functional groups can bind to a single molecule of the under-studied dye), and when (n=1) this condition signifies the attachment of the adsorbed species to an adsorption site in a non-parallel configuration, indicative of a mono-adsorbate process leading to the formation of a monomer [80].

Figure 9 shows the n values at four temperatures, 283, 293, 303, and 313 K, and the obtained values of this parameter are given in **Table 6.** The n1 values corresponding to the four temperatures were found as 2.7, 3.058, 2.342 and 2.721, while the n2 values are 0.452, 0.966, 7.411and 5.126 at 283, 293, 303 and 313, respectively. The MB–GP interaction revealed a vertical (non-parallel) arrangement with a multimolecular manner mechanism for the n_1. In addition, in the 2nd variable n_2 a vertical setting presented, a multimolecular mode for temperatures 283 and 293, the adsorbed MB attitude was changed to horizontal placement, and the molecule acquired a parallel (horizontal) orientation with a multi–docking mode by increasing the solution temperature to 303 and 313 K.

3.6.1.2. **Parameter N_m**

The density of the receptor site N_m parameter functions as a steric indicator, specifying the number of occupied adsorption sites within a unit mass of the adsorbent. Moreover, it denotes the number of available adsorption sites for species adsorbed at the state of equilibrium [81].

In **Figure 9**, the temperature-dependent variation in receptor site density (N_m) is depicted. The densities of the GP receptor sites, specifically N_{m1} and N_{m2}, exhibited a decreasing trend with the temperature rise. This phenomenon is correlated with an elevation in the quantity of

captured molecules (n_1 and n_2 per site), indicative of a heightened tendency toward aggregation as the temperature rises.

3.6.1.3. **Parameter Q_{sat}**

The saturation adsorption quantity, Q_{sat}, serves as a steric parameter interdependent with other steric factors ($Q_{sat,i}=N_{mi}*n_i$). In accordance with the most appropriate statistical physics model, Q_{sat} can be expressed in terms of the number of species adsorbed per adsorption site, the density of adsorption sites, and/or the formation of layers. This metric enables an assessment of the effectiveness of the adsorbent utilized in the adsorption process [82].

In **Figure 9**, the temperature-dependent variation of the overall saturation adsorption quantity was graphically represented. The total adsorbed amount at saturation exhibited a notable sensitivity to temperature fluctuations. Specifically, an elevation in temperature led to a decrease in the adsorbed quantity, attributable to the exothermic nature of the adsorption process a characteristic feature in conventional adsorption phenomena.

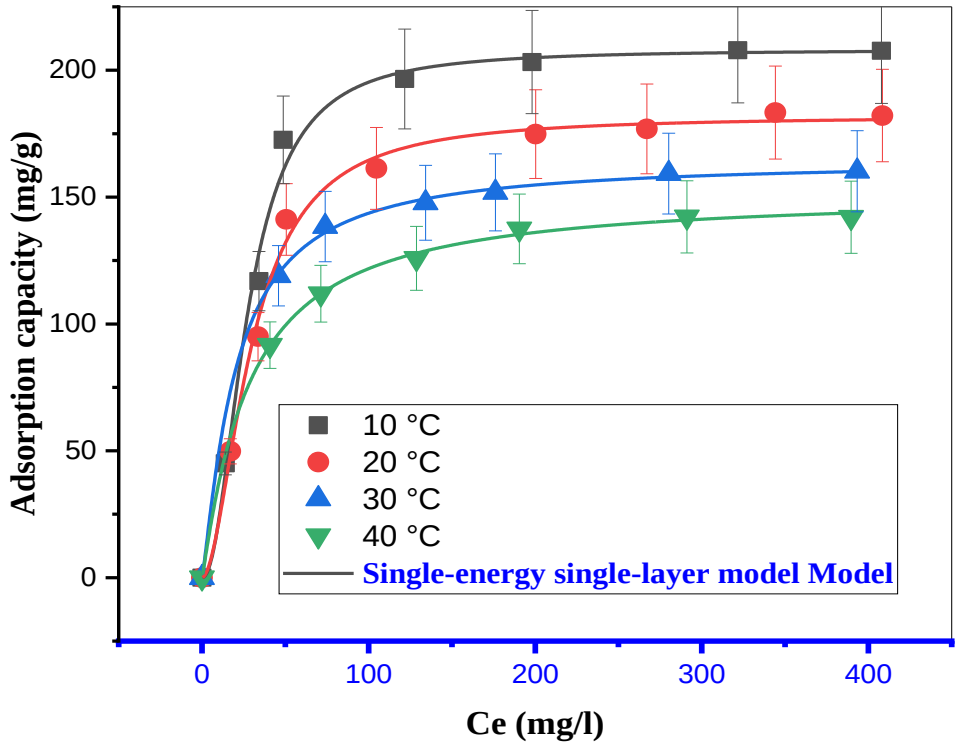

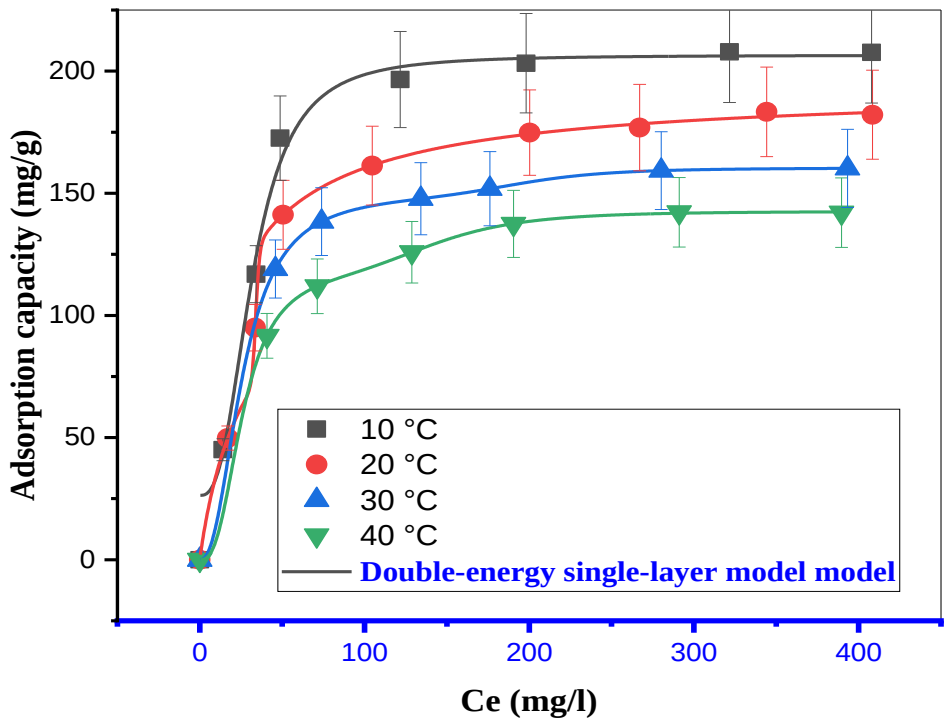

662

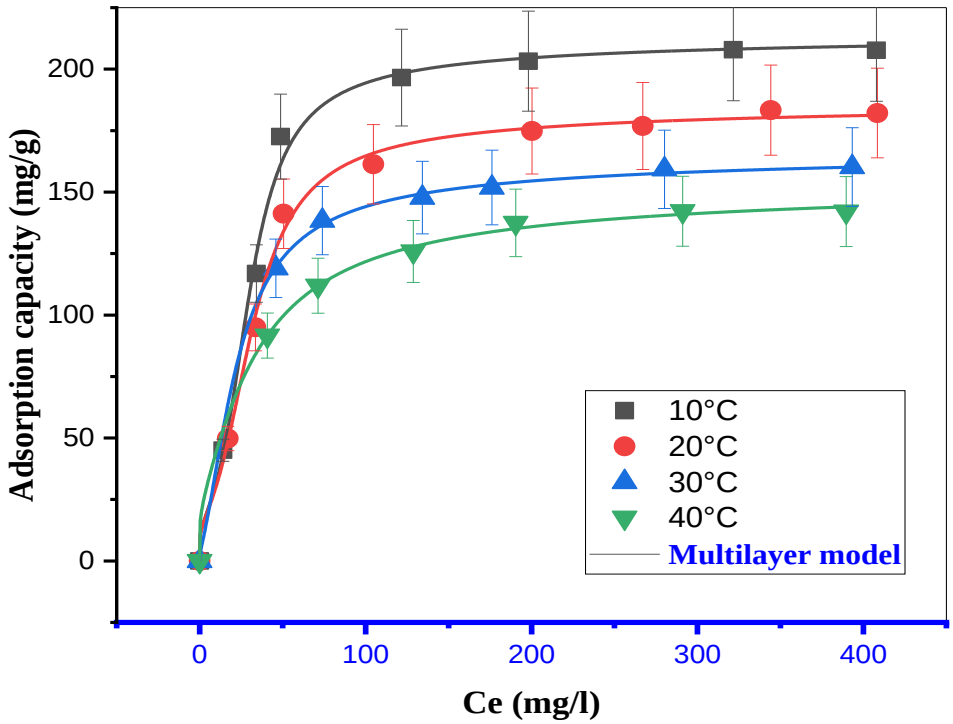

663

664 **Figure.8.** The outcome of fitting isotherm data pertaining to the adsorption of MB onto a GP

665 adsorbent with M1, M2, and M3 models (m = 15 mg. v = 25 ml. stirring = 250 ppm. pH=6.6).

666

667 **Table.6.** The determined parameter values for advanced models in the context of the

668 adsorption process of MB onto GP biomass.

Models	Parametrs	T = 283 K	T = 293 K	T = 303 K	313 K
M1	n	2.102	1.844	1.209	1.101
	N_m	98.981	98.642	135.976	137.628
	$C_{1/2}$	27.381	29.598	20.277	27.866
	R^2	**0.993**	**0.995**	**0.999**	**0.999**
M2	n_1	2.700	3.058	2.342	2.721
	n_2	0.452	0.966	7.411	5.126
	N_{m1}	66.716	64.158	43.494	1.861
	N_{m2}	142.174	58.234	4.727	1.377
	C_1	32.101	34.024	25.945	25.944
	C_2	$6.569*10^{-16}$	30.487	195.439	143.787
	R^2	**0.995**	**0.999**	**1**	**0.999**
M3	n	0.178	0.164	0.095	0.117
	N_{m1}	36.423	33.872	30.501	23.634
	N_{m2}	32.784	33.399	58.987	56.983
	C_1	$1.151*10^{-32}$	$3.737*10^{-34}$	$4.91*10^{11}$	$6.848*10^{-35}$
	C_2	30.957	33.193	18.847	34.896
	R^2	**0.995**	**0.996**	**0.999**	**0.999**

669

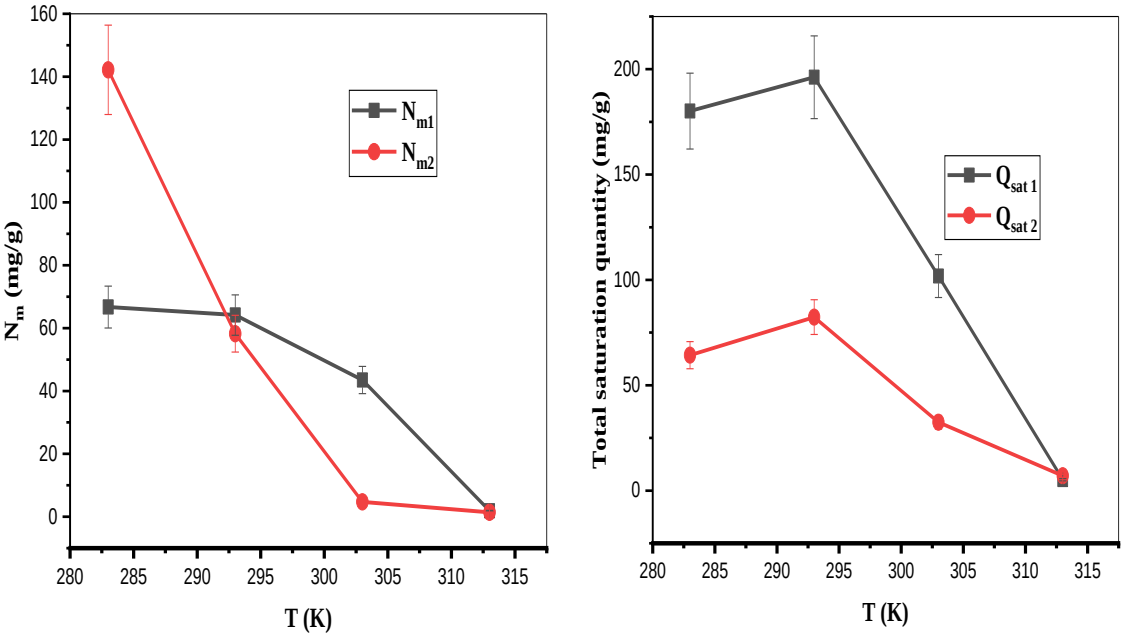

670

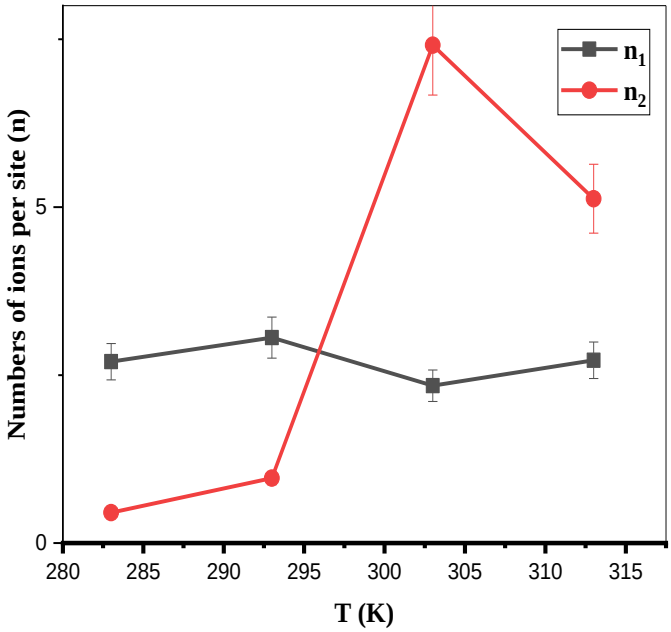

Figure.9. Changes in Nm, n, and Qsat with temperature during the adsorption process of MB-GP.

3.7. Thermodynamic

From **Table S2**, it is clear that the sorption of MB onto GP is exothermic, as shown by the negative value of H, supporting the findings on the temperature impact, which shows that the adsorption capacity falls as temperature rises. From 10 to 40 °C, ΔG° is positive and augmented, indicating that adsorption is viable at higher temperatures. At the solid-liquid interface during adsorption, the positive entropy ΔS° indicates an increase in randomness as indicated in **Table S2**.

The application of the advanced Double-energy single-layer model (M2) enables the computation of thermodynamic parameters, encompassing entropy, Gibbs free energy, and internal energy [83,84].

Table.7. The function of entropy, free enthalpy, and internal energy as related to the M2 model.

Function	Equation	Number
Entropy	$\frac{S_a}{K_B} = N_1\left[ln\left(1+\left(\frac{C_e}{C_1}\right)^{n_1 m}\right)+\frac{n_1 ln\left(\frac{C_1}{C_e}\right)}{1+\left(\frac{C_1}{C_e}\right)^{n_1 m}}\right]+N_2\left[ln\left(1+\left(\frac{C_e}{C_2}\right)^{n_2}\right)+\frac{n_2 ln\left(\frac{C_2}{C_e}\right)}{1+\left(\frac{C_2}{C_e}\right)^{n_2}}\right]$	**(29)**
Gibbs free enthalpy	$G = K_B T ln\left(\frac{C_e}{Z_v}\right)\left[\frac{Q_{sat1}}{1+(\frac{C_1}{C_e})^{n_1 m}}+\frac{Q_{sat2}}{1+(\frac{C_2}{C_e})^{m n_2}}\right]$ $Z_v = \frac{Z_{gtr}}{V} = \left(\frac{2\pi m K_B T}{h^2}\right)^{3/2}$	**(30)**
Internal energy	$E_{int} = K_B T\left[N_{1s}\frac{ln(\frac{C_e}{Z_v})+n_{1m}ln(\frac{C_1}{C_e})}{1+(\frac{C_1}{C_e})^{n_{1m}}}+N_{2s}\frac{ln(\frac{C_e}{Z_v})+n_2 m ln(\frac{C_2}{C_e})}{1+(\frac{C_2}{C_e})^{n_2 m}}\right]$	**(31)**

The computation of the Gibbs free enthalpy involves the utilization of **Equation (34)** as outlined in **Table 7**, relying on the M2. Subsequently, the Gibbs free enthalpy is graphically represented against adsorbate concentrations across diverse temperatures for the GP adsorbent, as illustrated in **Figure 10**. The observation in **Figure 10** indicates the negativity of the Gibbs free energy, signifying the spontaneous nature of the adsorption process. Furthermore, an increase in temperature is correlated with a diminishing free enthalpy, indicating a consequential reduction in the viability of the adsorption process [85].

The assessment of internal energy serves as a comprehensive means to evaluate all energy contributions to the MB adsorption system [48,84]. The general expression for internal energy is represented by **Equation (35)**. The depicted values for this thermodynamic parameter in the examined adsorption system are presented in **Figure 10**. Notably, all recorded internal energy values manifest as negative, indicative of the spontaneous occurrence of the Methylene Blue adsorption systems and the concurrent release of energy.

The entropy variation for M2 model given by **Equation (33)**, exhibits two distinct behaviors discernible in terms of concentration. At lower concentrations ($C_{1/2} > C$), there is an observed increase in entropy, indicating a rise in molecular disorder. This implies that MB

molecules undergo random movement across the biosorbent (GP) surfaces, facilitated by the abundant active sites provided by GP at low concentrations, enhancing the adsorption process. Conversely, at higher concentrations ($C_{1/2}$ < C), an opposite phenomenon is evident. The elevation in concentration results in a reduction of entropy. This decline is attributed to a plausible decrease in the number of receptor sites available on GP for adsorption as the concentration increases [84,85].

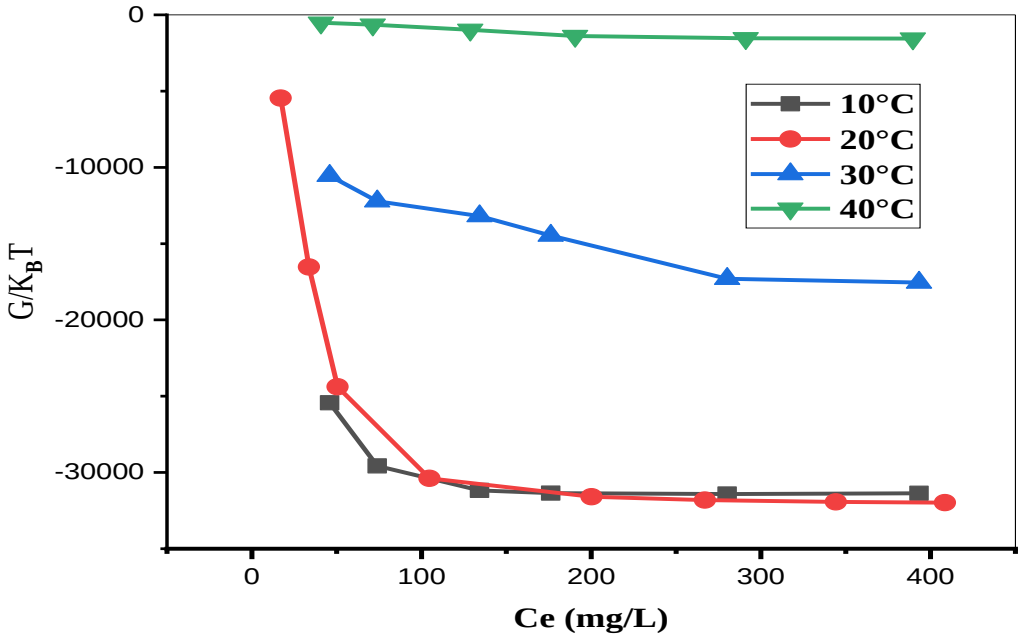

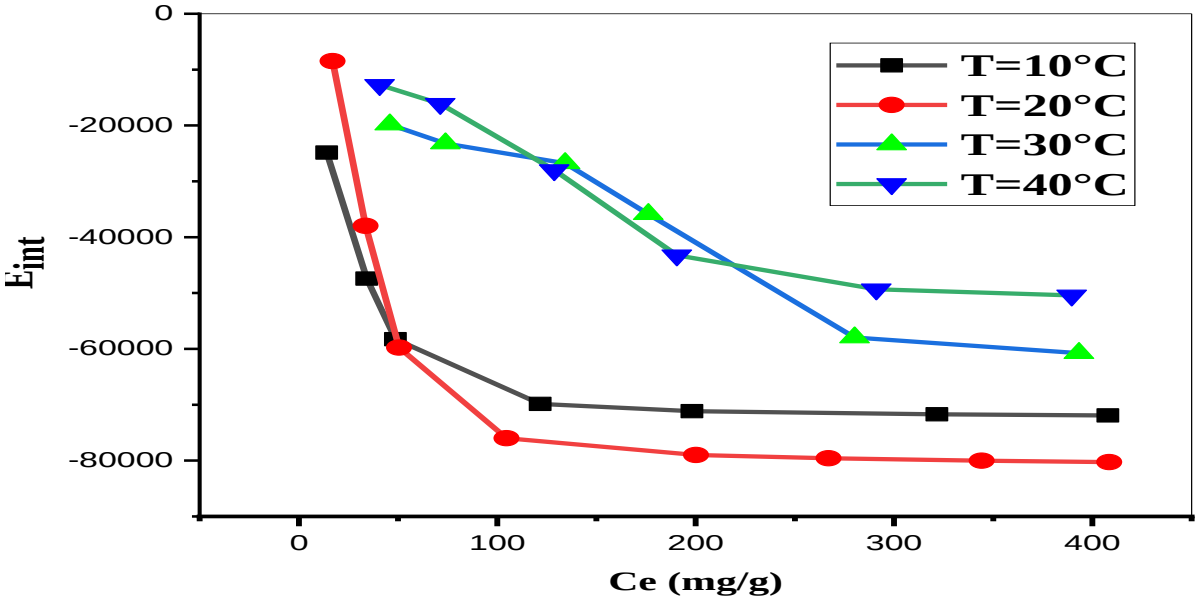

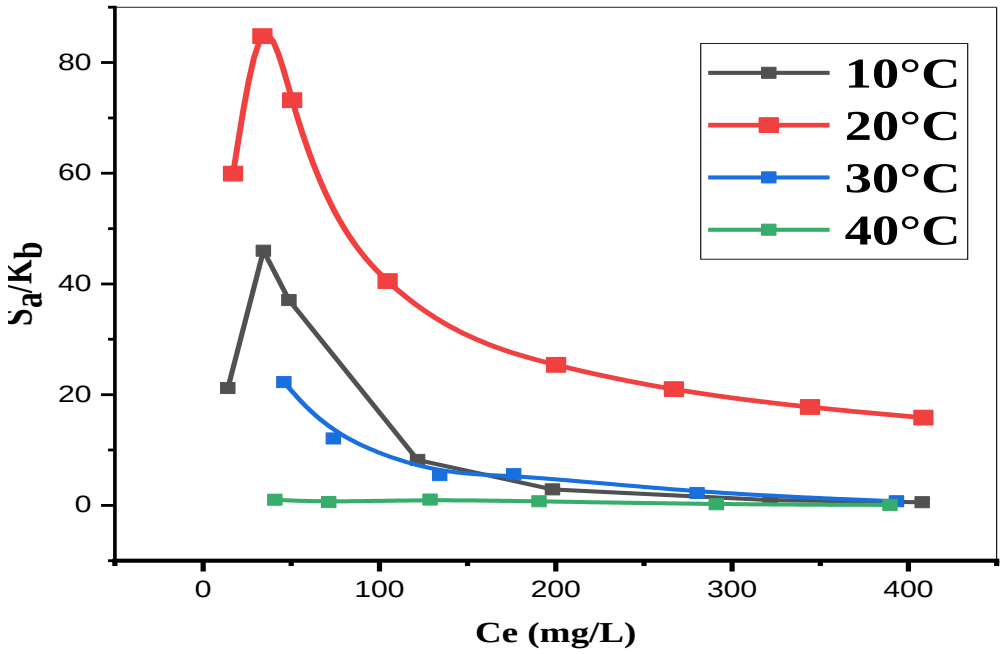

Figure.10. Evolution of entropy, free enthalpy, and internal energy as a function of concentration during the absorption of MB by GP adsorbent at distinct temperatures.

3.8. Density Function Theory (DFT) study

Quantum chemical parameters	MB	GP
E_{Tot} (ev)	-1181.86	-4104.31
E_{HOMO} (ev)	-3.870	0.423
E_{LUMO} (ev)	-2.684	0.268
ΔE^{Gap} (ev)	1.186	-0.155
η (ev)	-0.593	0.07751
X (ev)	6.554	-0.691
S (ev)	-0.843	6.4516
ω (ev)	-36.218	3.0805
σ (ev)	-1.686	12.903
ΔN_{max} (ev)	-11.05	-8.916

As widely recognized, the propensity of a molecule to undergo electron loss is frequently associated with its highest occupied molecular orbital energy (E_{HOMO}), whereas the molecule's capacity to accept electrons, as well as its lowest unoccupied molecular orbital energy (E_{LUMO}), are closely tied to its electron affinity [47,53].

Furthermore, a diminutive energy gap (E_{GAP}) signifies heightened reactivity within the molecule, thereby enhancing the efficacy of MB adsorption onto the GP surface, thereby manifesting a notably stable adsorption process.

The concept of global hardness encapsulates a molecule's resistance to deformations or polarization when subjected to minor perturbations in chemical reactions. In general, molecules characterized by low global hardness values and elevated global softness values exhibit greater ease in adhering to suitable surfaces. The capacity of molecules to attract electrons is also demonstrated by the electrophilicity index, which can rise with falling values.

	MB	**GP**
A	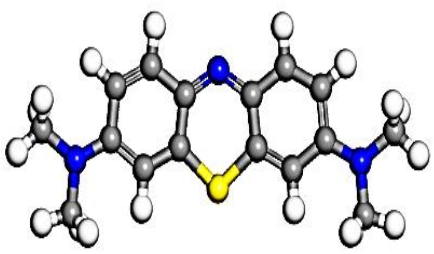	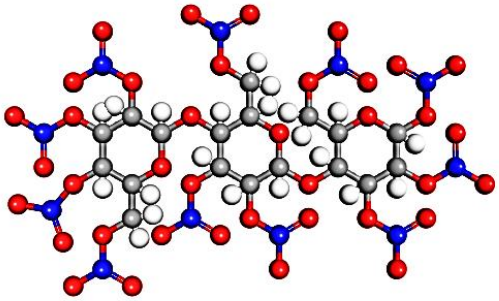
B	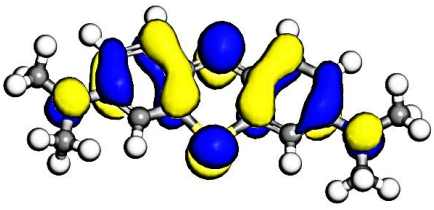	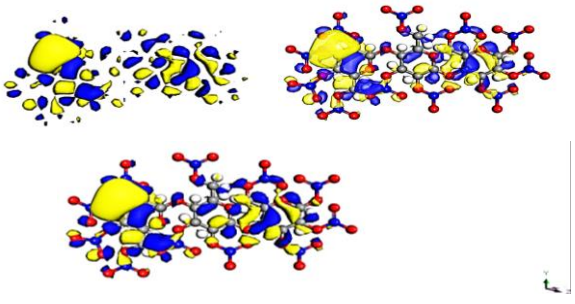
C	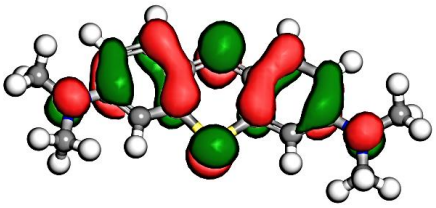	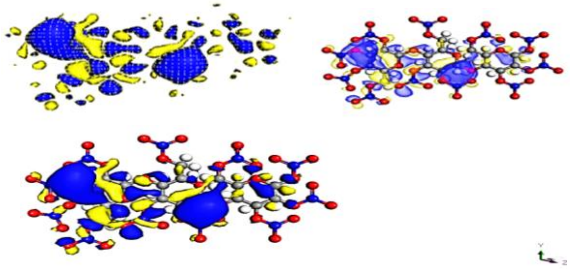

d

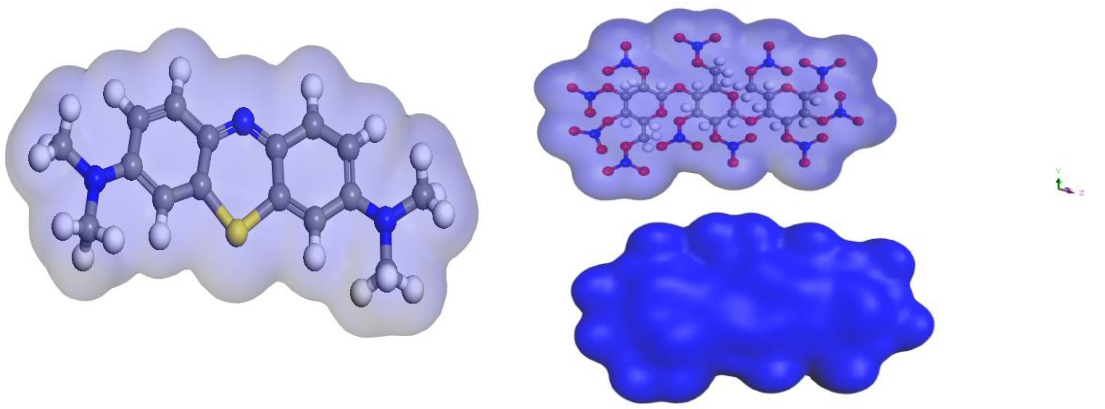

Figure.11. (a) Optimized molecular structure, (b) HOMO, (c) LUMO and (d) electron density.

3.9. Molecular Dynamic Simulation study

A pivotal approach for elucidating the intricate interactions between MB molecules and the adsorbent (GP) surface involves leveraging molecular dynamic simulations (MDS). The MDS-based investigation reveals that the equilibrium configuration of MB adsorption onto the GP (-1 0 0) surface, as illustrated in **Figure 12**, corresponds to the most thermodynamically stable state. **Figure 12** depicts the parallel adsorption mode of MB molecules on the GP (-1 0 0) surface, which underscores the strong intermolecular contacts between MB and the GP surface atoms. The chemical adsorption of MB onto the GP surface can be attributed to the contribution of electron-rich atoms, specifically sulfur, nitrogen, and oxygen, as inferred from a comprehensive analysis of the molecular structures of both MB and GP. Furthermore, Van der Waals dispersion is crucial in enabling and facilitating the capture of MB molecules onto the cellulose surface, which aligns with the outcomes obtained during the isoelectric point characterization, confirming physical adsorption. The computational assessment of various adsorption energy parameters for MB onto the GP surface is concisely presented in **Table 8**. The observed negative adsorption energy value (-75.821 kcal/mol) underscores the fact that the adsorption procedure is spontaneous. The notably elevated binding energy value (37.117

kcal/mol) can be attributed to a superior and highly stable adsorption process. It is noteworthy that the deformation energy associated with the molecular rearrangements induced by MB adsorption implies a reduction in the stability of both the MB molecules and the GP surface.

In summary, molecular dynamic simulations serve as a pivotal tool for gaining a comprehensive understanding of the complex interplay between MB molecules and the GP surface [86]. The adsorption process is primarily governed by chemical interactions involving electron-rich atoms, and it is further enhanced by Van der Waals forces, culminating in a stable adsorption configuration. Thermodynamic analysis, as succinctly conveyed in **Table S2**, underscores the spontaneity and favorability of the adsorption process, with the deformation energy indicating the stability implications arising from MB-induced conformational changes.

Table.8. Energies derived from computational calculations pertaining to the adsorption of MB molecules onto the GP surface.

Adsorption energy, Kcal/mol	**Rigid adsorption energy, Kcal/mol**	**Deformation energy, Kcal/mol**	**BM: d Fad/dNi**	**Total energy, Kcal/mol**
-75.821	-85.69	9.868	-75.821	-143.212

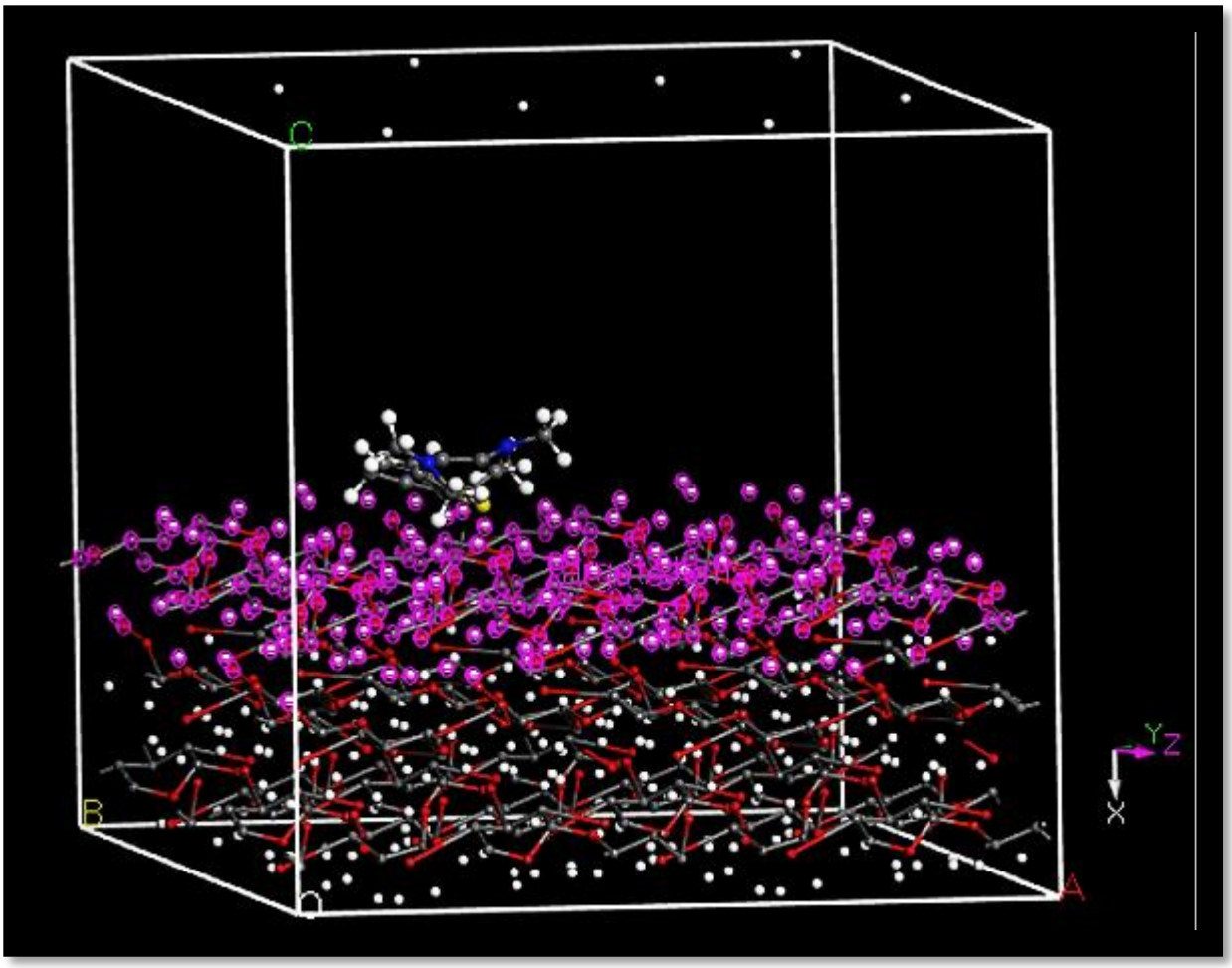

Figure.12. The arrangement of MB's equilibrium adsorption onto the GP surface.

3.10. Regenerative Characteristics

The recyclable properties of the adsorbent material played a pivotal role in the assessment of its applicability. The regenerative performance of GP in the context of MB adsorption is depicted in **Figure 13**. It is obvious that both have the ability for adsorption and desorption efficiency exhibited a diminishing trend with an increasing number of usage cycles. During the first four cycles, GP retained substantial adsorption efficacy, demonstrating adsorption capacities (mg/g) and removal rates (%) of 80.92, 60.84, 43, and 35.75 mg/g for cycles 1 to 4 respectively, constituting 78.75%, 59.20%, 41.84%, and 34.78% of the initial values. Nonetheless, after five cycles, the adsorption capacity of the adsorbent decreased to 13.26 mg/g. This decline is related to the incomplete desorption of MB from the adsorption sites, when MB

molecules are not fully released from these sites, they continue to occupy space on the biosorbent surface, limiting its capacity to adsorb more MB molecules, resulting in a decrease in the adsorption capability of the GP. Consequently, the optimal usage cycle for GP was determined to be five cycles.

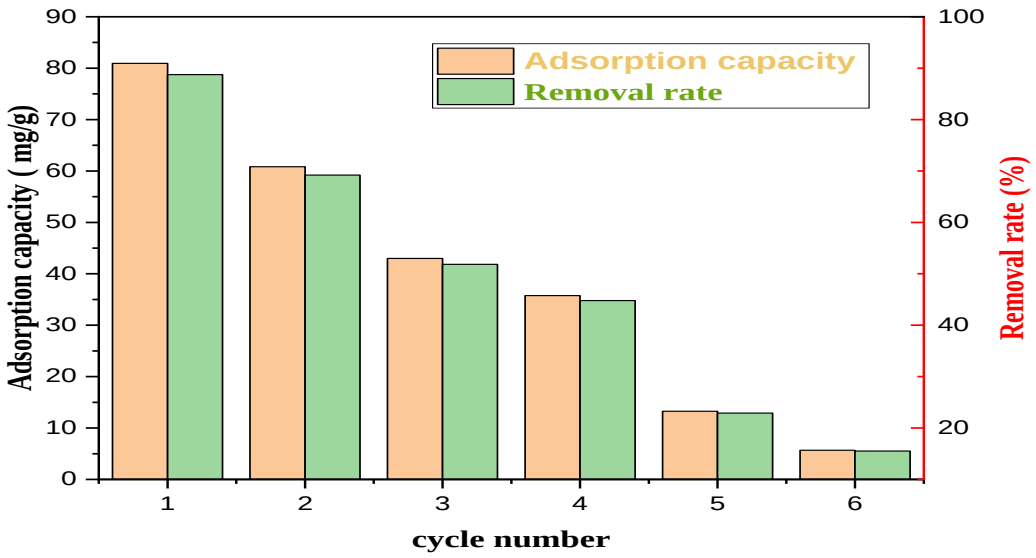

Figure.13. Assessment of the Durability and Reusability of GP for MB Adsorption. Experimental Parameters: MB Solution (100 mg/L), T= Room Temperature, GP Mass= 50 mg, Time: 1 hour.

3.11. Gaussian Process Regression coupled with Lévy flight distribution

After optimizing ten kernel functions using the LFD algorithm in conjunction with the base function, the most effective kernel function was selected based on statistical criteria. **Table 9** presents the outcomes of this selection process, offering details on the best model, its corresponding parameters (kernel scale and sigma), and performance assessments using statistical metrics (R and RMSE) across three distinct phases (training, validation, and all data). The table also includes information on kernel settings, the preferred kernel function, resulting basis functions, the count of Lévy flights employed, and the number of iterations required to achieve the best model.

Table.9. Performances of the GPR-LFD model.

LFD	**Max_iteration=50** **SearchAgents_no=100**											
	Kernel function	***Basis Function***	***Kernel Scale***		***Sigma***	**Quantity**	**R**			**RMSE**		
			Sigma M	**SigmaF**			**Train**	**Val**	**ALL**	**Train**	**Val**	**ALL**
GPR_DA	***ARD-Exponential***	PureQuadratic	11.9415 25.4642 22.5696 28.4045 89.6149	134.7677	0.5744	65	1.0000	0.9980	0.9990	0.0142	3.1874	2.5390

The results obtained following the optimization of kernel functions and basis functions highlight the superiority of the model using the ARD exponential kernel with the PureQuadratic basis compared to other kernels listed in **Table 9**. It is important to note that the parameters of the LFD were set to Max_iteration=50 and SearchAgents_no=100.

In terms of performance metrics, the correlation coefficients demonstrate an exceptional fit of the model to the data. The correlation coefficient for the training set reaches a perfect value of 1.0000, indicating an optimal correlation. For the validation set, the high correlation coefficient of 0.9980 emphasizes a robust agreement with the validation data. The overall correlation coefficient, which stands at 0.9990, attests to an outstanding overall performance of the model.

Regarding the RMSE, measuring the difference between predicted and actual values, the results are equally remarkable. The RMSE for the training set is 0.0142, indicating high accuracy in predicting training data. For the validation set, the RMSE remains remarkably low at 3.1874, confirming the robustness of the model in predicting validation data. The overall RMSE, established at 2.5390, reflects a satisfactory overall performance of the model across all data.

The optimized model with the ARD exponential kernel and Pure Quadratic basis stands out for its excellent fit to the data, characterized by high correlation coefficients and exceptionally low

prediction errors, both for the training and validation sets. These results underscore the reliability and precision of the model in predicting the adsorbed quantities of MB by GP, reinforcing its significant potential for advanced predictive applications.

These results are visually presented in **Figure 14**, providing a graphical representation of the findings.

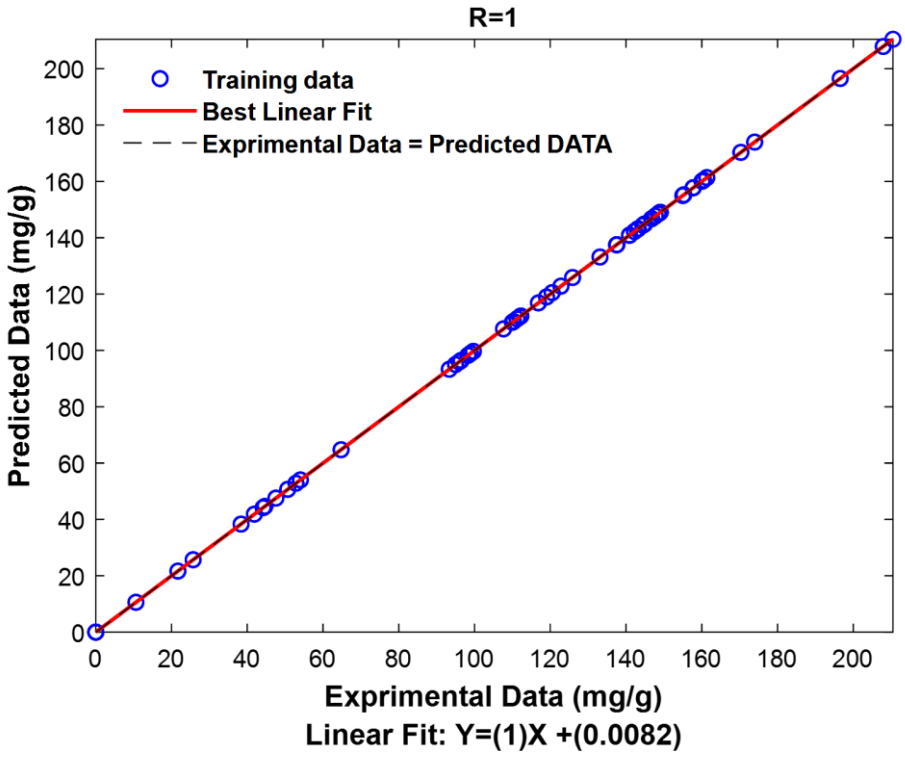

(a)

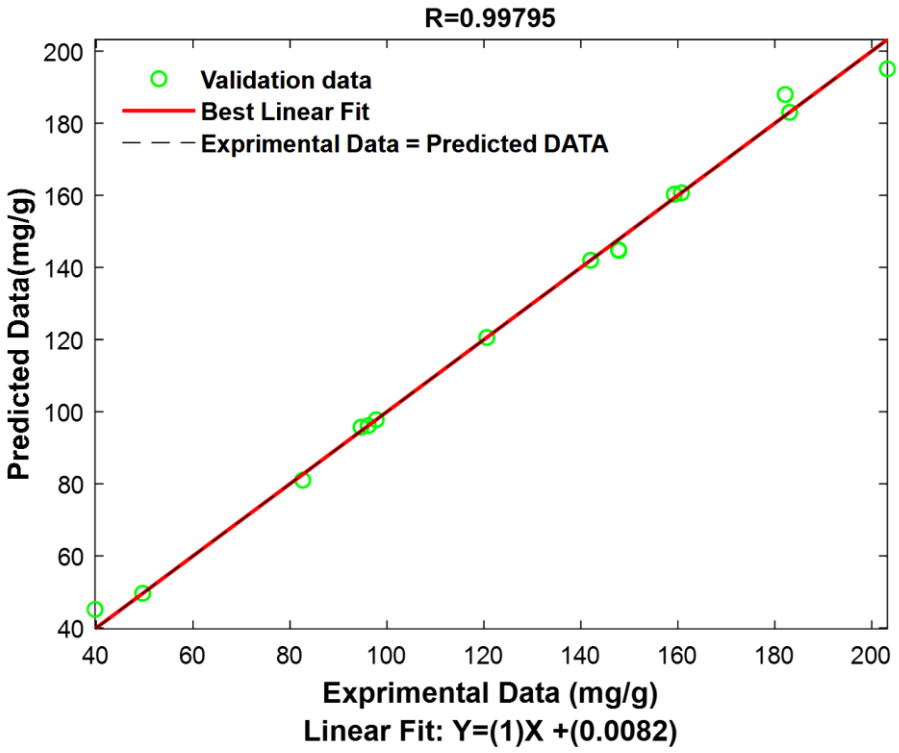

(b)

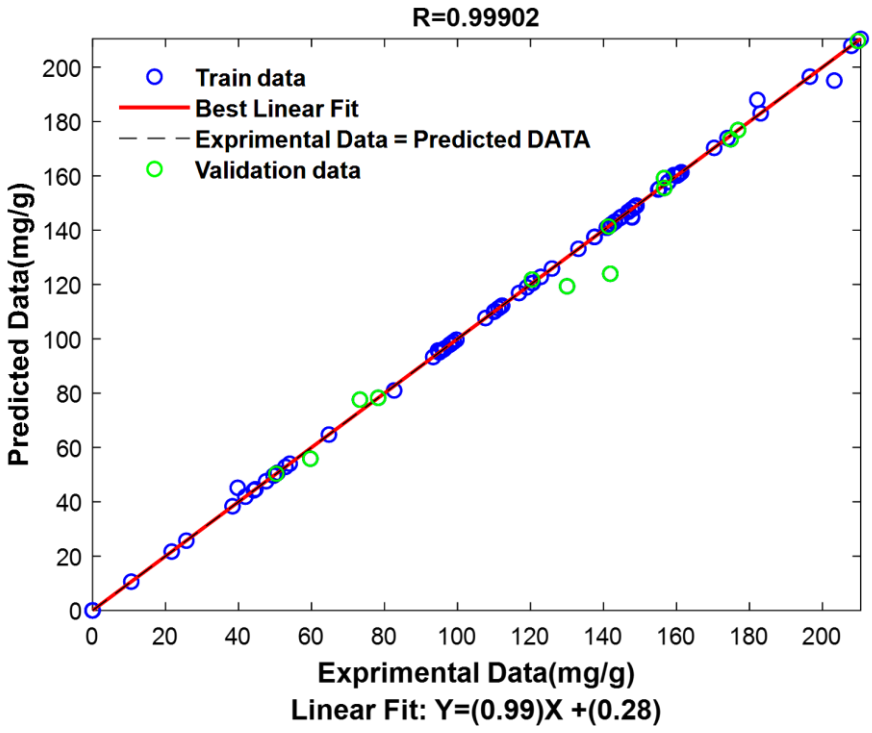

(c)

Figure.14. Relationship between the experimental and the GPR_LFD model predicted values: (a) training Data, (b) validation Data, and (c) All Data

3.11.1. Performance of GPR_LFD model tested

In the initial phase of data partitioning, a deliberate reservation of 15% from the database was specifically earmarked for assessing the GPR_LFD model's top performance achieved through interpolation. The outcomes of this thorough evaluation have been meticulously documented in **Table 10**, providing a comprehensive presentation of statistical coefficients and their corresponding errors.

Table.10. Model test performance of GPR_LFD.

R	RMSE
0.9952	3.8513

The results from **Table 10** reveal the outstanding performance of the GPR_LFD model during its evaluation of the test data. A remarkably high correlation coefficient of 0.9952 attests to a robust positive correlation between the model predictions and the actual values. Furthermore, the low RMSE of 3.8513 indicates notable accuracy, with model predictions exhibiting an average error margin of approximately 3.85 units compared to the actual values. These findings confirm the GPR_LFD model's ability to accurately and reliably capture underlying relationships in the data, underscoring its relevance and efficacy in the context of interpolating test data.

To provide a visual representation of these performances, experimental values and predicted values have been graphically represented in **Figure 15**.

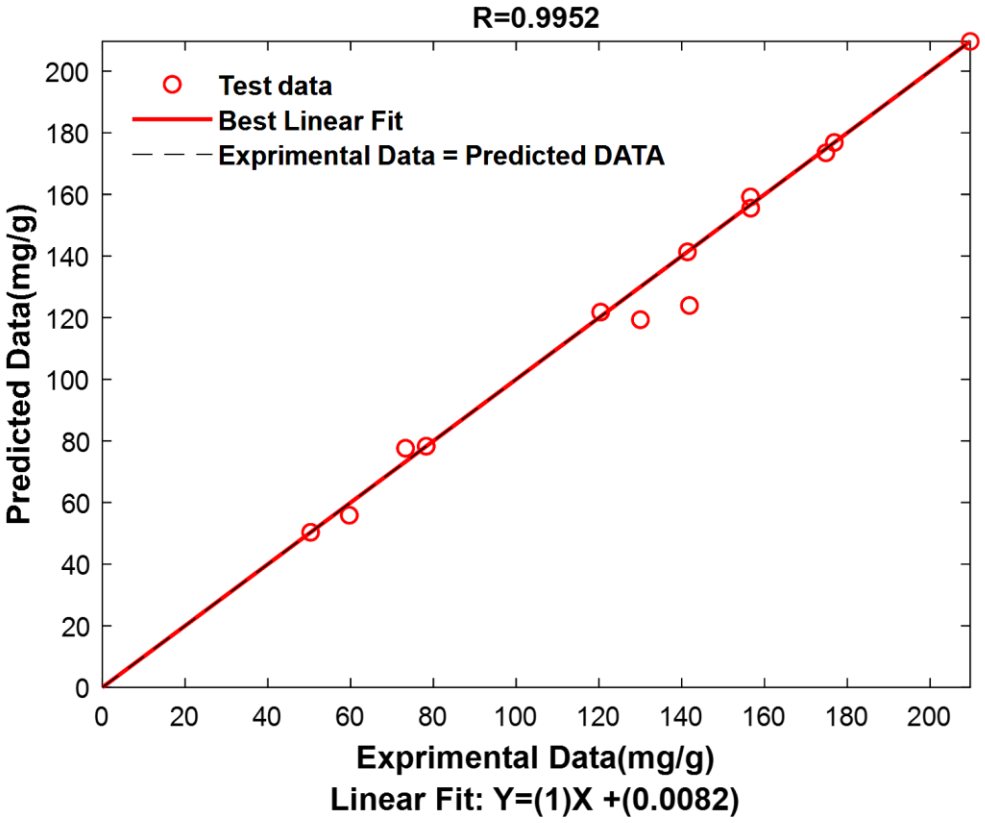

Figure.15. Comparison between experimental and predicted values to assess performance OF GPR_LFD.

3.11.2. Residues study

In this section, a rigorous and comprehensive evaluation was conducted to thoroughly assess the performance and efficacy of the selected model [66,87]. This in-depth assessment encompassed both the application of the residual method and an error histogram, spanning various critical phases, including training, validation, and testing [61,65]. Following this, a meticulous comparative analysis was performed by superimposing experimental values onto predicted ones, covering all data points across the training, validation, and testing datasets, vividly depicted in **Figure 16(a)**. Furthermore, an extensive error quantification involved a scrupulous examination of the disparities between experimental and predicted values for the entire dataset, including data from the training, validation, and testing sets, adhering to

established methodologies. The outcomes of this thorough error assessment were thoughtfully visualized in **Figure 16(b)**, employing advanced residual analysis techniques.

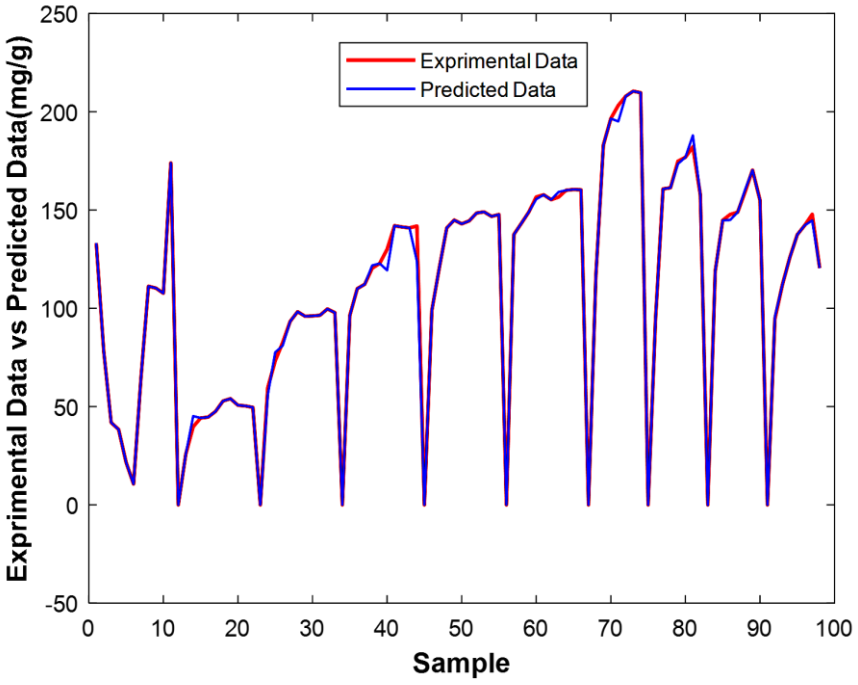

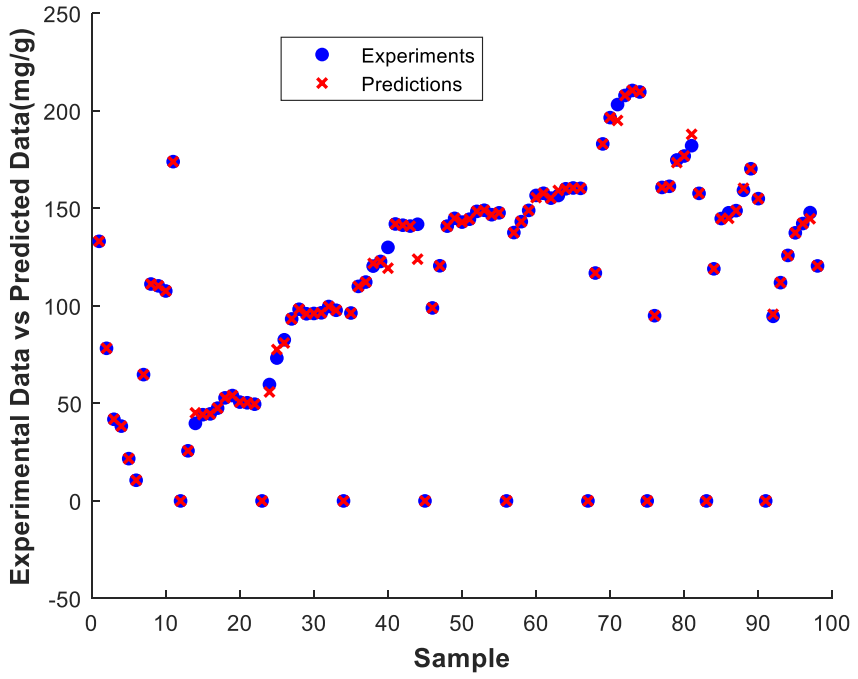

(a)

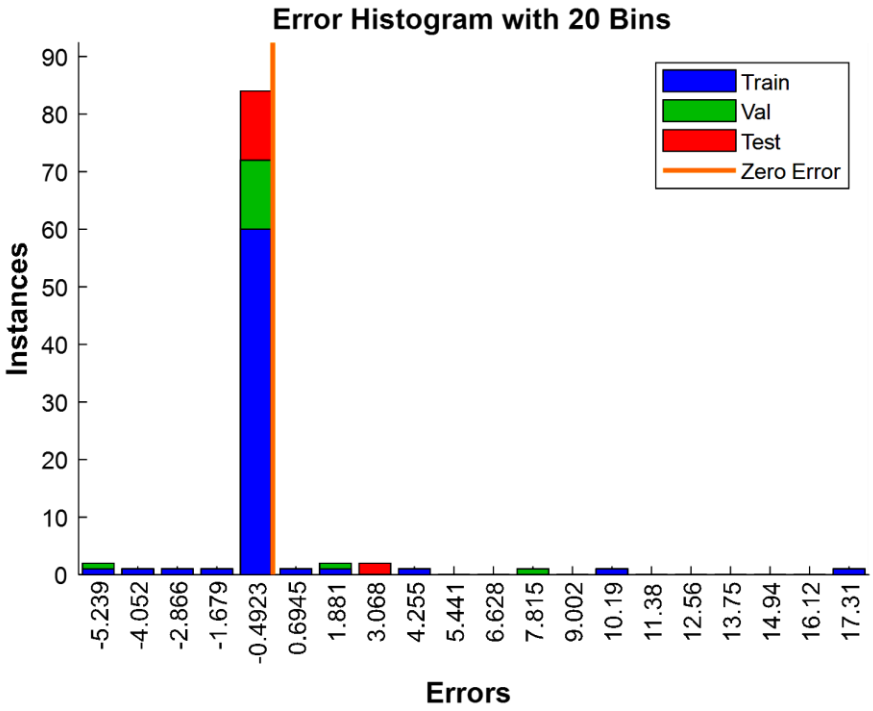

(b)

Figure.16. Residuals relating to the models established by the different techniques according to the estimated values: (a) Relationship between experimental data and the predicted data of samples, and (b) Instances distribution of errors.

The findings depicted in **Figure 16a** gracefully emphasize a substantial agreement between experimental and predicted values, providing compelling validation of the model's effectiveness. Moreover, **Figure 16b** offers additional persuasive evidence of the model's efficiency, with 84 out of 98 experimental values closely aligning with their predicted counterparts, resulting in only minor deviations. Notably, the residual errors for the remaining 14 cases were exceptionally minimal, further highlighting the model's outstanding performance. These comprehensive observations unequivocally establish the model's robustness and precision, leaving no room for doubt about its capabilities.

3.12. Optimization and Validation of the optimum conditions

The optimization of independent parameters for maximizing MB uptake was carried out using the Lévy flight distribution method [57]. The accuracy of the optimization results was then rigorously validated through laboratory experiments. The comparative analysis in **Table 11** intricately presents predicted values alongside experimental results, offering a comprehensive view of the corresponding errors between the two datasets.

Where: $\text{Error} = \text{Experimental response} - \text{Predicted response}$ **(32)**

Table.11. Comparison between actual and predicted responses at optimum conditions.

GPR_LFD	
• X_1 = 30 min. X_2 = 0.6 g. X_3= 400 mg/L, X4= 6.6 and X5= 10°C	
MB uptake (mg/g). experimental values	207.90
MB uptake (mg/g). predicted values	207.89
Error (mg/g)	0.008

The results prominently showcase a compelling alignment between the observed outcomes and the predictions derived from the GPR_LFD model in the domain of MB adsorption. Under the precisely defined optimal conditions—characterized by a 30-minute contact time, 0.600 g of adsorbent mass, an initial MB concentration of 400 mg/L, a pH level of 6.6, and a temperature of 10°C, the experimental MB adsorption rate reached an impressive 207.90 mg/g. Remarkably, the model-predicted value closely mirrored this at 207.89 mg/g, with a minute discrepancy of only 0.008 mg/g. This nuanced precision in the concordance between predicted and observed values vividly underscores the LFD algorithm's exceptional efficacy in orchestrating optimization with remarkable finesse.

These findings not only affirm the reliability of the GPR_LFD model but also underscore the algorithm's inherent ability to guide the optimization process with precision. The LFD algorithm's seamless convergence on optimal conditions, resulting in such close correspondence between experimental and predicted values, attests to its robustness and efficiency in navigating intricate parameter spaces. This detailed congruence further instills confidence in the model's capacity to capture complex patterns and optimize outcomes accurately, solidifying its value as a powerful tool in the realm of MB adsorption studies.

3.13. Interface for optimization and prediction

At the forefront of advancements in computational tools for environmental research, an innovative MATLAB application has been meticulously engineered to harness the formidable capabilities of the LFD algorithm. This application serves a dual purpose by not only optimizing process conditions but also predicting MB uptake with precision, employing the sophisticated GPR_LFD model. A hallmark of user-friendliness, this cutting-edge tool seamlessly integrates the computational prowess of MATLAB with the intricate workings of the LFD algorithm.

Users can effortlessly input a spectrum of experimental parameters, including contact time, adsorbent mass to initial MB concentration, pH, and temperature. This dynamic interface empowers the LFD algorithm to dynamically optimize these conditions, refining them to their optimal configurations. Beyond this, the application utilizes the GPR_LFD model to predict MB uptake with a high degree of accuracy, facilitating a comprehensive understanding of adsorption behavior under various scenarios. What sets this application apart is not only its functionality but also its intuitive user interface, allowing researchers and practitioners to explore diverse scenarios effortlessly. The real-time visualization of how different parameters impact MB adsorption enhances its usability. This innovative MATLAB application emerges as a powerful, efficient, and user-centric tool, embodying the seamless integration of LFD

optimization and GPR_LFD prediction, making it indispensable for researchers in the dynamic field of MB adsorption studies.

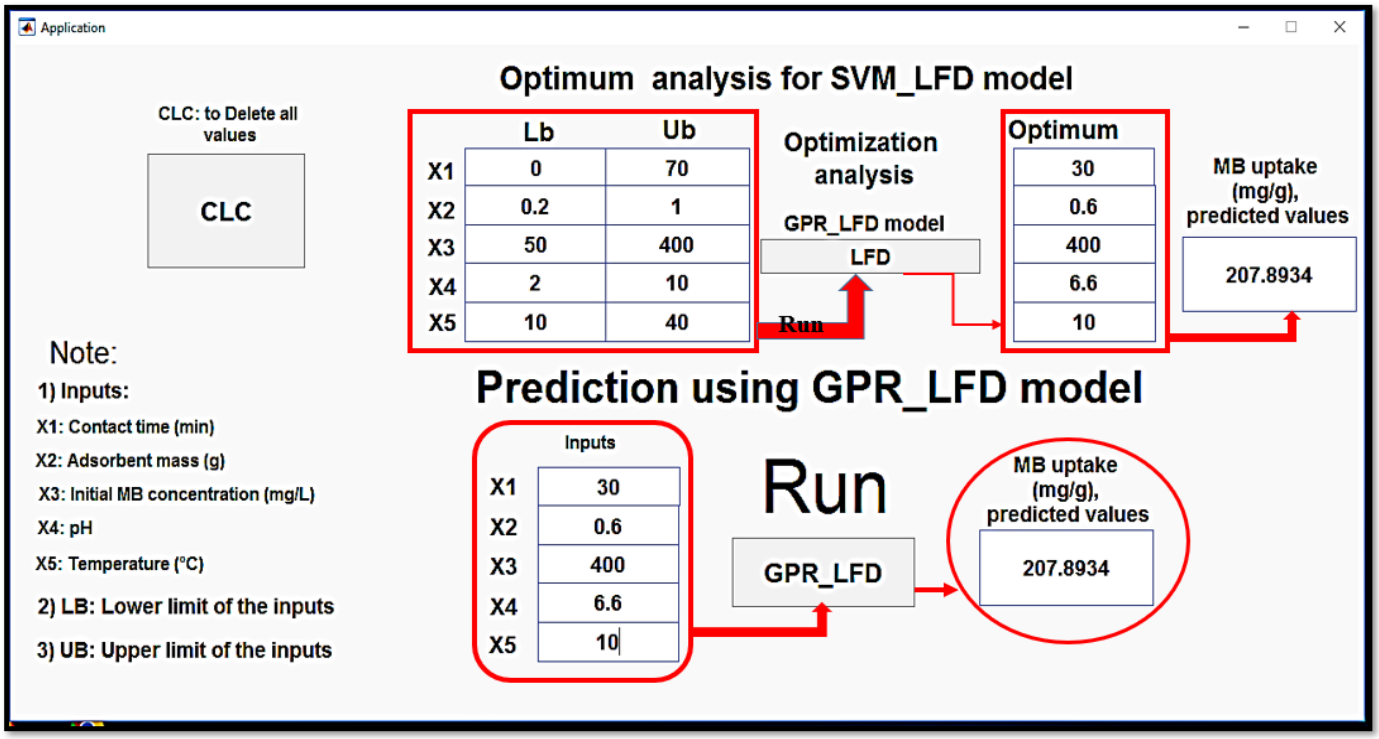

Figure.17. MATLAB Interface for optimization analysis (LFD) and prediction of MB uptake using GPR_LFD.

3.14. Comparison with Published Results: A Comparative Analysis

The **Table 12** provides a comparison of the maximum adsorption capacities of various adsorbents, expressed in milligrams per gram (mg/g). Among the listed adsorbents, the biocomposite film derived from cellulose demonstrates a maximum adsorption capacity of 146.81 mg/g. This highlights the adsorption capabilities of this material, indicating its potential for water contaminant removal. The tea-derived activated material (AST) shows a slightly lower adsorption capacity, at 104.2 mg/g. Although this value is lower than that of the biocomposite film of cellulose, it remains significant, suggesting the effectiveness of AST as an adsorbent. On the other hand, the sludge-rice husk biochar exhibits a more modest adsorption

capacity, at 22.59 mg/g. However, it still serves as a potentially useful adsorbent, especially considering its biological origin and availability. The jute stick biomass stands out with an impressive adsorption capacity of 198.86 mg/g, making it one of the most efficient adsorbents on the list. This high adsorption capacity underscores the effectiveness of jute stick biomass for water contaminant removal. The banana stem-activated carbon shows an adsorption capacity of 64.66 mg/g, making it a reasonable choice for various water purification applications, although it is less efficient than jute stick biomass. Macore fruit shells exhibit the lowest adsorption capacity among the listed adsorbents, with a value of 10.61 mg/g. While this is the lowest value listed, it remains significant in certain application contexts. Lastly, the "GP" developed in this study stands out with a remarkable adsorption capacity of 207.89 mg/g, the highest among all the mentioned adsorbents. This high value suggests that the "GP" could be a highly effective adsorbent for water contaminant removal, offering new prospects for treating contaminated water.

Table.12. Comparative Assessment of Adsorption Capacities for MB Dye among Various Adsorbents.

Adsorbent name	**Capacity maximum (mg/g)**	**Reference**
Biocomposite film derived from cellulose	146.81	[88]
Tea-derived activated material (AST)	104.2	[89]
Sludge-rice husk biochar	22.59	[90]
Jute stick biomass	198.86	[91]
Banana stem-activated carbon	64.66	[92]
Macore fruit shells	10.61	[93]
GP	207.89	This work

In conclusion, the data from the table reveal that the "GP" exhibits the highest adsorption capacity among all listed adsorbents. This remarkable performance suggests that the "GP" could

be an extremely effective adsorbent for treating contaminated water, thereby providing new opportunities to enhance water purification technologies. These findings underscore the importance of research on advanced materials such as the "GP" in seeking sustainable solutions to challenges related to access to clean water.

3.15. Proposal for an adsorption mechanism

Figure 18 provides a visual representation of the interactions involved in the adsorption process of cationic methylene blue dye onto the biosorbent. Understanding the mechanism behind the adsorption of organic compounds onto the adsorbent requires a comprehensive analysis, typically involving a comparison of the FTIR spectra of the adsorbent before and after the adsorption process. This analysis is often supplemented by studies conducted under various conditions such as pH, temperature, and initial dye concentration, as well as desorption experiments. These investigations, combined with FTIR analysis and MDS results, allow researchers to propose the primary adsorption mechanisms. The identified mechanisms typically include electrostatic attraction, dipole-dipole interactions, Yoshida hydrogen bonding formations, and n-π interactions. Specifically, the primary adsorption process for various aromatic contaminants on carbonaceous materials is often attributed to the n-π electron interaction. In this process, the aromatic rings of pollutant molecules act as electron acceptors, while carbonyl oxygen ions on the biochar surface serve as electron donors. Through spectral analysis, researchers observe a significant reduction in the intensity of the band at 1623 cm^{-1}, associated with C=O functional groups, after adsorption, indicating the involvement of n-π interactions in the adsorption process. Hydrogen bonding interactions also play a crucial role in adsorption and can be classified into two types. Firstly, dipole-dipole hydrogen bonds frequently form between appropriate atoms (e.g., oxygen or nitrogen) of the aromatic adsorbates and surface hydrogen atoms of hydroxyl groups on the carbonaceous material. Secondly, Yoshida hydrogen bonding connections typically occur between the aromatic rings of adsorbate molecules and the surface hydroxyl groups of the carbonaceous material. Spectral analysis post-adsorption shows a slight decrease in the intensity of bands associated with C-O and -OH groups, suggesting the presence of dipole-dipole and Yoshida hydrogen bonding interactions. Overall, understanding these complex interactions is essential for elucidating the adsorption mechanisms and optimizing the adsorption process for efficient removal of contaminants from water sources.

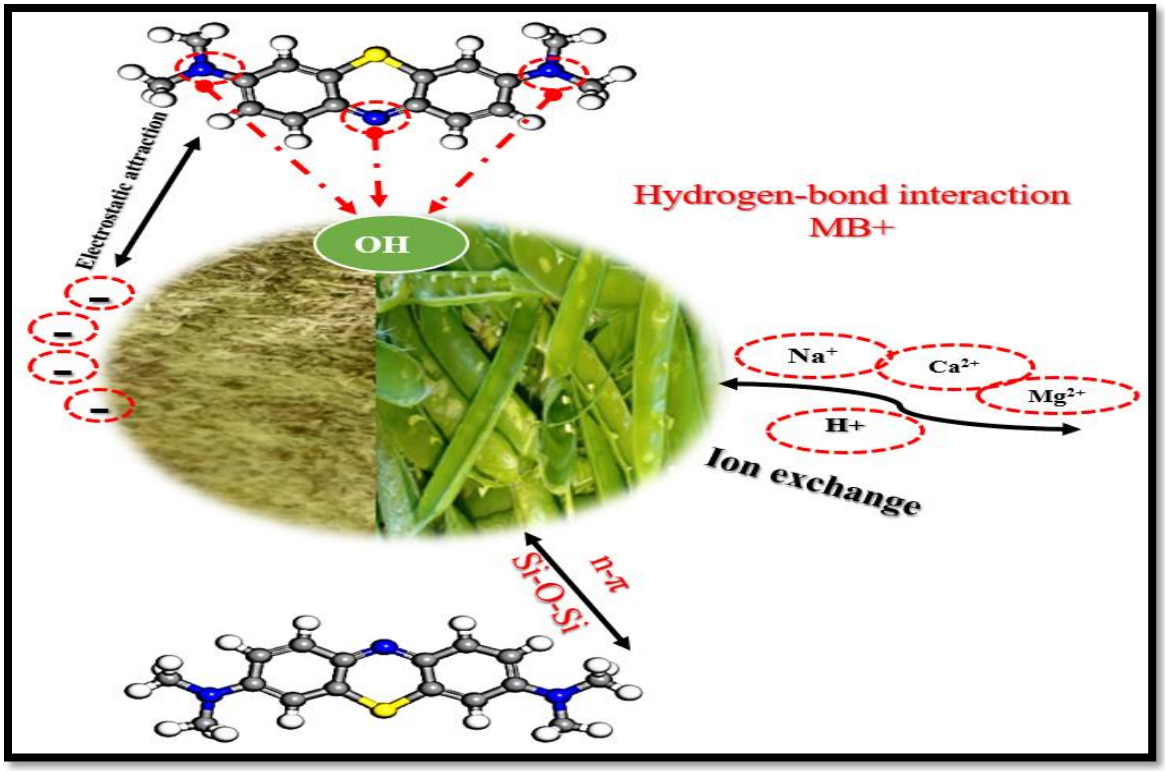

Figure.18. Adsorption mechanism of MB onto GP absorbent.

3.16. Cost Analysis for natural GP biosorbent Synthesis

The Energy and Cost Estimate section provides a meticulous breakdown of the financial aspects associated with the production of natural green pea peels (GP) biosorbent. This analysis aims to offer a comprehensive prediction of the anticipated production costs involved in generating one kilogram of GP biosorbent. **Table 13** in the section presents a detailed cost estimation of the various stages involved in the production process. The first item listed is the "Cost of peels collection," which is intriguingly noted as 0.00 USD. This indicates that there are no direct expenses incurred in collecting the pea peels, suggesting that they are obtained as a byproduct, potentially from food processing industries or agricultural activities. This approach not only minimizes production costs but also underscores the sustainability of utilizing agricultural waste for value-added purposes. Moving on, the "Cost of drying of adsorbent" is also listed as 0.00 USD, with a note specifying that the drying process utilizes natural sunlight. By leveraging solar energy for drying, the production process avoids the need for energy-intensive methods,

significantly reducing operational expenses. This environmentally friendly approach not only contributes to cost-effectiveness but also aligns with sustainable practices. The final cost item in **Table 13** is "Milling and sieving," which incurs a total cost of 100 w. The cost is expressed in terms of power consumption, with 1 kW/h equivalent to 0.035 USD in Algeria. This cost likely represents the electricity consumption associated with milling and sieving equipment used to process the pea peels into the desired biosorbent form. Despite this expense, the overall cost remains relatively low, further enhancing the economic viability of the production process.

In summary, the cost estimation provided in **Table 13** offers valuable insights into the financial aspects of GP biosorbent production. The absence of expenses for peels collection and drying, coupled with the utilization of solar energy and relatively low milling and sieving costs, highlights the cost-effectiveness and sustainability of the production process. This comprehensive cost analysis serves as a valuable tool for decision-makers and stakeholders, facilitating informed decisions regarding resource allocation and investment in GP biosorbent production for efficient and environmentally friendly water treatment solutions. According to these results, a comparison of its costs with current studies is presented in **Table S3**.

Table.13. cost estimation of GP biosorbent.

unit	Total cost
Cost of peels collection	0.00 USD
Cost of drying of adsorbent	0.00 USD (dried using the sun)
Milling and sieving	100 w (1KW/h = 0.035 USD in Algeria)

4. Conclusion

This research presents a comprehensive exploration of the Methylene Blue (MB) adsorption dynamics onto Green Peel (GP), employing diverse methodologies from statistical physics

models to Molecular Dynamic Simulation (MDS). The study firmly establishes GP's suitability for adsorption, substantiated by analyses like X-ray diffraction (XRD) and Fourier-transform infrared spectroscopy (FT-IR), The Brunauer-Emmett-Teller (BET), providing a robust foundation for subsequent investigations. By dissecting influential factors in MB removal such as adsorbent mass, pH, concentration, and temperature, the research furnishes crucial insights into the nuances of the adsorption process.

Isotherm data analysis identifies the double-energy single-layer model as the most fitting, supported by comprehensive correlation coefficient evaluation. Steric parameters reveal intricate adsorption geometry and mechanisms, with temperature-dependent variations shedding light on captivating shifts in orientation and modes. Thermodynamic scrutiny exposes the exothermic nature of MB adsorption onto GP, coupled with a noticeable decline in adsorption capacity at elevated temperatures. Density Function Theory (DFT) studies deepen our understanding of the interaction, reactivity, and stability of both MB and GP systems. These studies emphasize the potential for electron transfer during adsorption. In the desorption process, electron transfer between the MB dye and the ethanol solvent plays a crucial role in facilitating the release of MB molecules from the adsorption sites on the biosorbent. When a suitable electron acceptor or donor is present in the system, it provides a pathway for electron transfer to occur more efficiently. This can happen through various mechanisms, such as redox reactions, where the electron donor transfers electrons to the MB dye, promoting its desorption from the biosorbent surface. Conversely, electron acceptors can accept electrons from the MB dye, facilitating its release into the solvent. Overall, the presence of suitable electron donors or acceptors enhances the kinetics of the desorption process, leading to more effective removal of MB from the biosorbent material. On the other hand, while regenerative properties underscore GP's recyclability, albeit with diminishing efficiency over successive usage cycles, Molecular Dynamics Simulation (MDS) unveils the stable adsorption configuration of MB onto the GP

surface. This approach elucidates the intricate interplay of chemical interactions and Van der Waals forces. Density Function Theory (DFT) studies deepen our understanding of the interaction, reactivity, and stability of both MB and GP systems. These studies emphasize the potential for electron transfer during adsorption. In the desorption process, electron transfer between the MB dye and the ethanol solvent plays a crucial role in facilitating the release of MB molecules from the adsorption sites on the biosorbent. On the other hand, while regenerative properties underscore GP's recyclability, albeit with diminishing efficiency over successive usage cycles, Molecular Dynamics Simulation (MDS) unveils the stable adsorption configuration of MB onto the GP surface. This approach elucidates the intricate interplay of chemical interactions and Van der Waals forces. Harnessing Gaussian Process Regression coupled with Lévy flight distribution (GPR_LFD), the study optimizes kernel functions, pinpointing the ARD exponential kernel and PureQuadratic basis as optimal choices. Rigorous model testing attests to its precision, reliability, and exceptional alignment with the data. Experimental validation under optimized parameters (30-minute contact time, 0.600 g adsorbent mass, initial MB concentration of 400 mg/L, pH 6.6, and 10°C) yields a striking congruence between experimental and predicted MB uptake values, reaching an impressive 207.90 mg/g. A user-friendly MATLAB interface integrates LFD optimization and GPR prediction for practical application. In essence, this research bridges empirical observations with advanced modeling techniques, advancing our understanding of MB adsorption onto GP and emphasizing GP's substantial potential as an effective adsorbent. The study not only contributes to scientific understanding but also hints at future applications in environmental remediation and wastewater treatment, showcasing the synergy between empirical investigation and computational modeling in unraveling complex phenomena.

Nomenclature

C the intercept of Intraparticle diffusion function

1059	C_o	initial concentration of MB ($mg \cdot L^{-1}$)
1060	Ce	final concentration of MB in the solution
1061	C_t:	concentration of MB at time t ($mg \cdot L^{-1}$)
1062	$C_{1/2}$	the concentration at half–saturation ($mg \cdot L^{-1}$)
1063	C_1	concentrations at half saturation for the first active site ($mg \cdot L^{-1}$)
1064	C_2	concentrations at half saturation for the second active site ($mg \cdot L^{-1}$)
1065	E_{int}	System internal energy ($J \cdot mol^{-1}$)
1066	F	fraction of MB adsorbed at time t
1067	G	Gibbs free enthalpy ($J \cdot mol^{-1}$)
1068	GP	Green pea
1069	h	Planck constant (J•s-1)
1070	K_B	Boltzmann constant (J•K)
1071	k_1	equilibrium rate constant of PFO equation ($L \cdot min^{-1}$)
1072	k_2	equilibrium rate constant of PSO equation ($L \cdot min^{-1}$)
1073	K_F	Freundlich constant (g•L•mg)
1074	K_{id}	the rate constant of intraparticle diffusion($mg \cdot g\text{-}1 \cdot min^{-0.5}$)
1075	K_L	Langmuir constant ($L \cdot mg^{-1}$)
1076	k_n	equilibrium rate constant of PNO equation ($L \cdot min^{-1}$)
1077	K_s	Sips constant ($L \cdot mg^{-1}$)
1078	M	mass of the mixture (g)
1079	m_s	the exponent of the Sips model
1080	MB	methylene blue
1081	n	number of ions per site
1082	n1	number of ions per site for the first site receptor
1083	n2	number of ions per site for the second site receptor
1084	nf	Freundlich (R-P) constant
1085	no	biosorption reaction order N number of experimental points performed
1086	Nm	sites receptor density($mg \cdot g^{-1}$)
1087	PFO	pseudo-first-order,
1088	PSO	pseudo-second-order

PNO pseudo-nth-order

Qe amount of dye adsorbed at equilibrium ($mg \cdot g^{-1}$)

Qt quantity adsorbed at time t ($mg \cdot g^{-1}$)

R the correlation coefficient

RMSE Root Mean Squared Error

Sa Entropy ($J \cdot mol \cdot K^{-1}$) t time (min)

T temperature (°C or °K)

V volume of the mixture (L)

Z_v Translation partition function per unit volume

Z_{gtr} translation partition function

β the constant of desorption (g/mg).

α the constant of initial sorption rate (mg/(g·min))

ϑ the fractional power kinetic model constant.

Acknowledgement

The author Salah Knani extend his appreciation to the Deanship of Scientific Research at Northern Border University, Arar, KSA for funding this research work through the project number "NBU-FFR-2024-2483-09"

References

[1] A. Mammeri, A. Tiri, L. Belkhiri, H. Salhi, D. Brella, E. Lakouas, H. Tahraoui, A. Amrane, L. Mouni, Assessment of surface water quality using water quality index and discriminant analysis method, Water 15 (2023) 680.

[2] A.G. Adeniyi, J.O. Ighalo, Biosorption of pollutants by plant leaves: An empirical review, J. Environ. Chem. Eng. 7 (2019) 103100. https://doi.org/10.1016/j.jece.2019.103100.

[3] Md.T.-A. Hassan, M. Hossain, M. Hossain, Mechanism of Basic Violet 3 Adsorption on Used Black Tea Leaves from Neutral Solution, (2007).

[4] A. Stavrinou, C.A. Aggelopoulos, C.D. Tsakiroglou, Exploring the adsorption mechanisms of cationic and anionic dyes onto agricultural waste peels of banana, cucumber and potato: Adsorption kinetics and equilibrium isotherms as a tool, J. Environ. Chem. Eng. 6 (2018) 6958–6970. https://doi.org/10.1016/j.jece.2018.10.063.

[5] N.T. Abdel-Ghani, G.A. El-Chaghaby, E.-S.A. Rawash, E.C. Lima, Magnetic activated carbon nanocomposite from Nigella sativa L. waste (MNSA) for the removal of Coomassie brilliant blue dye from aqueous solution: Statistical design of experiments for optimization of the adsorption conditions, J. Adv. Res. 17 (2019) 55–63. https://doi.org/10.1016/j.jare.2018.12.004.

[6] C. Pearce, J. Lloyd, J. Guthrie, The removal of colour from textile wastewater using whole bacterial cells: a review, Dyes Pigments 58 (2003) 179–196.

[7] M. Benjelloun, Y. Miyah, G. Akdemir Evrendilek, F. Zerrouq, S. Lairini, Recent Advances in Adsorption Kinetic Models: Their Application to Dye Types, Arab. J. Chem. 14 (2021) 103031. https://doi.org/10.1016/j.arabjc.2021.103031.

[8] Y. Dai, Q. Sun, W. Wang, L. Lu, M. Liu, J. Li, S. Yang, Y. Sun, K. Zhang, J. Xu, Utilizations of agricultural waste as adsorbent for the removal of contaminants: A review, Chemosphere 211 (2018) 235–253.
[9] S. Yadav, A. Yadav, N. Bagotia, A.K. Sharma, S. Kumar, Adsorptive potential of modified plant-based adsorbents for sequestration of dyes and heavy metals from wastewater - A review, J. Water Process Eng. 42 (2021) 102148. https://doi.org/10.1016/j.jwpe.2021.102148.
[10] T. Maneerung, J. Liew, Y. Dai, S. Kawi, C. Chong, C.-H. Wang, Activated carbon derived from carbon residue from biomass gasification and its application for dye adsorption: Kinetics, isotherms and thermodynamic studies, Bioresour. Technol. 200 (2016) 350–359. https://doi.org/10.1016/j.biortech.2015.10.047.
[11] S. Pandey, E. Fosso-Kankeu, J. Ramontja, Efficient and rapid adsorption characteristics of templating xanthan gum-graft-poly (aniline) and silica nanocomposite toward removal of toxic methylene blue dyes, in: 2017: pp. 27–28.
[12] A.H. Jawad, A. Kadhum, Y. Ngoh, Applicability of dragon fruit (Hylocereus polyrhizus) peels as low-cost biosorbent for adsorption of methylene blue from aqueous solution: Kinetics, equilibrium and thermodynamics studies, Desalination Water Treat. 109 (2018). https://doi.org/10.5004/dwt.2018.21976.
[13] K. Madi, D. Chebli, H. Ait Youcef, H. Tahraoui, A. Bouguettoucha, M. Kebir, J. Zhang, A. Amrane, Green Fabrication of ZnO Nanoparticles and ZnO/rGO Nanocomposites from Algerian Date Syrup Extract: Synthesis, Characterization, and Augmented Photocatalytic Efficiency in Methylene Blue Degradation, Catalysts 14 (2024) 62.
[14] H. Tahraoui, S. Toumi, M. Boudoukhani, N. Touzout, A.N.E.H. Sid, A. Amrane, A.-E. Belhadj, M. Hadjadj, Y. Laichi, M. Aboumustapha, Evaluating the Effectiveness of Coagulation–Flocculation Treatment Using Aluminum Sulfate on a Polluted Surface Water Source: A Year-Long Study, Water 16 (2024) 400.
[15] A.N.E.H. Sid, H. Tahraoui, M. Kebir, M.A. Bezzekhami, B. Kouini, A.H. Hassein-Bey, T. Selma, A. Amrane, A. Imessaoudene, L. Mouni, Comparative investigation of the effect of eggshellpowder and calcium carbonate as additivesin eco-friendly polymer drilling fluids, Sustainability 15 (2023) 3375.
[16] M. Smara, R. Khalladi, N. Moulai-Mostefa, K. Madi, D. Mansour, S. Lekmine, O. Benslama, H. Tahraoui, J. Zhang, A. Amrane, Efficiency of Hydrogen Peroxide and Fenton Reagent for Polycyclic Aromatic Hydrocarbon Degradation in Contaminated Soil: Insights from Experimental and Predictive Modeling, Processes 12 (2024) 621.
[17] M.I. Kanjal, M. Muneer, M.A. Jamal, T.H. Bokhari, A. Wahid, S. Ullah, A. Amrane, A. Hadadi, H. Tahraoui, L. Mouni, A Study of Treatment of Reactive Red 45 Dye by Advanced Oxidation Processes and Toxicity Evaluation Using Bioassays, Sustainability 15 (2023) 7256.
[18] S.S. Shah, T. Sharma, B.A. Dar, R.K. Bamezai, Adsorptive removal of methyl orange dye from aqueous solution using populous leaves: Insights from kinetics, thermodynamics and computational studies, Environ. Chem. Ecotoxicol. 3 (2021) 172–181. https://doi.org/10.1016/j.enceco.2021.05.002.
[19] R. Kumar, M.A. Barakat, Decolourization of hazardous brilliant green from aqueous solution using binary oxidized cactus fruit peel, Chem. Eng. J. 226 (2013) 377–383. https://doi.org/10.1016/j.cej.2013.04.063.
[20] N.D. Shooto, C.S. Nkutha, N.R. Guilande, E.B. Naidoo, Pristine and modified mucuna beans adsorptive studies of toxic lead ions and methylene blue dye from aqueous solution, South Afr. J. Chem. Eng. 31 (2020) 33–43. https://doi.org/10.1016/j.sajce.2019.12.001.
[21] K.K. Wong, C.K. Lee, K.S. Low, M.J. Haron, Removal of Cu and Pb by tartaric acid modified rice husk from aqueous solutions, Chemosphere 50 (2003) 23–28. https://doi.org/10.1016/S0045-6535(02)00598-2.
[22] A. Guediri, A. Bouguettoucha, D. Chebli, N. Chafai, A. Amrane, Molecular dynamic simulation and DFT computational studies on the adsorption performances of methylene blue in aqueous solutions by orange peel-modified phosphoric acid, J. Mol. Struct. 1202 (2020) 127290.

[23] A. Guediri, A. Bouguettoucha, D. Chebli, A. Amrane, The use of encapsulation as a proposed solution to avoid problems encountered with conventional materials in powder form: Application in methylene blue removal from aqueous solutions, J. Mol. Liq. 316 (2020) 113841. https://doi.org/10.1016/j.molliq.2020.113841.
[24] T. Yumak, Surface characteristics and electrochemical properties of activated carbon obtained from different parts of Pinus pinaster, Colloids Surf. Physicochem. Eng. Asp. 625 (2021) 126982. https://doi.org/10.1016/j.colsurfa.2021.126982.
[25] H. Ait Ahsaine, M. Zbair, Z. Anfar, Y. Naciri, R. El haouti, N. El Alem, M. Ezahri, Cationic dyes adsorption onto high surface area 'almond shell' activated carbon: Kinetics, equilibrium isotherms and surface statistical modeling, Mater. Today Chem. 8 (2018) 121–132. https://doi.org/10.1016/j.mtchem.2018.03.004.
[26] C. Djama, D. Chebli, A. Bouguettoucha, I. Doudou, A. Amrane, Statistical physics modelling of azo dyes biosorption onto modified powder of Acorus calamus in batch reactor, Biomass Convers. Biorefinery 13 (2023) 1013–1028. https://doi.org/10.1007/s13399-020-01190-2.
[27] R. Aravindhan, J.R. Rao, B.U. Nair, Application of a chemically modified green macro alga as a biosorbent for phenol removal, J. Environ. Manage. 90 (2009) 1877–1883.
[28] F. Sakr, S. Alahiane, A. Sennaoui, M. Dinne, I. Bakas, A. Assabbane, Removal of cationic dye (Methylene Blue) from aqueous solution by adsorption on two type of biomaterial of South Morocco, Mater. Today Proc. 22 (2020) 93–96. https://doi.org/10.1016/j.matpr.2019.08.101.
[29] Y. Miyah, A. Lahrichi, M. Idrissi, Removal of cationic dye -Methylene bleu- from aqueous solution by adsorption onto corn cob powder calcined, 7 (2016) 96–104.
[30] N. Bouchelkia, H. Tahraoui, A. Amrane, H. Belkacemi, J.-C. Bollinger, A. Bouzaza, A. Zoukel, J. Zhang, L. Mouni, Jujube stones based highly efficient activated carbon for methylene blue adsorption: Kinetics and isotherms modeling, thermodynamics and mechanism study, optimization via response surface methodology and machine learning approaches, Process Saf. Environ. Prot. 170 (2023) 513–535. https://doi.org/10.1016/j.psep.2022.12.028.
[31] M. Zamouche, M. Chermat, Z. Kermiche, H. Tahraoui, M. Kebir, J.-C. Bollinger, A. Amrane, L. Mouni, Predictive Model Based on K-Nearest Neighbor Coupled with the Gray Wolf Optimizer Algorithm (KNN_GWO) for Estimating the Amount of Phenol Adsorption on Powdered Activated Carbon, Water 15 (2023) 493.
[32] M. Sadi, M. Soleimani, Development of artificial intelligence-based models for prediction of vanadium adsorption onto activated carbon nanocomposites, J. Water Process Eng. 55 (2023) 104220.
[33] C.E. Onu, B.N. Ekwueme, P.E. Ohale, C.P. Onu, C.O. Asadu, C.C. Obi, K.T. Dibia, O.O. Onu, Decolourization of bromocresol green dye solution by acid functionalized rice husk: artificial intelligence modeling, GA optimization, and adsorption studies, J. Hazard. Mater. Adv. 9 (2023) 100224.
[34] L.M.C. Oliveira, H. Koivisto, I.G. Iwakiri, J.M. Loureiro, A.M. Ribeiro, I.B. Nogueira, Modelling of a pressure swing adsorption unit by deep learning and artificial Intelligence tools, Chem. Eng. Sci. 224 (2020) 115801.
[35] N. Hamri, A. Imessaoudene, A. Hadadi, S. Cheikh, A. Boukerroui, J.-C. Bollinger, A. Amrane, H. Tahraoui, H.N. Tran, A.O. Ezzat, Enhanced Adsorption Capacity of Methylene Blue Dye onto Kaolin through Acid Treatment: Batch Adsorption and Machine Learning Studies, Water 16 (2024) 243.
[36] T. Mekhalif, K. Guediri, A. Reffas, D. Chebli, A. Bouguettoucha, A. Amrane, Effect of acid and alkali treatments of a forest waste, *Pinus brutia* cones, on adsorption efficiency of methyl green, J. Dispers. Sci. Technol. 38 (2017) 463–471. https://doi.org/10.1080/01932691.2016.1178585.
[37] S. Farch, M.M. Yahoum, S. Toumi, H. Tahraoui, S. Lefnaoui, M. Kebir, M. Zamouche, A. Amrane, J. Zhang, A. Hadadi, Application of Walnut Shell Biowaste as an Inexpensive Adsorbent for Methylene Blue Dye: Isotherms, Kinetics, Thermodynamics, and Modeling, Separations 10 (2023) 60.

[38] J. Lan, Y. Dong, Y. Sun, L. Fen, M. Zhou, H. Hou, D. Du, A novel method for solidification/stabilization of Cd(II), Hg(II), Cu(II), and Zn(II) by activated electrolytic manganese slag, J. Hazard. Mater. 409 (2021) 124933. https://doi.org/10.1016/j.jhazmat.2020.124933.
[39] A. Imessaoudene, S. Cheikh, A. Hadadi, N. Hamri, J.-C. Bollinger, A. Amrane, H. Tahraoui, A. Manseri, L. Mouni, Adsorption performance of zeolite for the removal of congo red dye: Factorial design experiments, kinetic, and equilibrium studies, Separations 10 (2023) 57.
[40] M. Kebir, H. Tahraoui, M. Chabani, M. Trari, N. Noureddine, A.A. Assadi, A. Amrane, N. Ben Hamadi, L. Khezami, Water Cleaning by a Continuous Fixed-Bed Column for Cr (VI) Eco-Adsorption with Green Adsorbent-Based Biomass: An Experimental Modeling Study, Processes 11 (2023) 363.
[41] S.H. Chien, W.R. Clayton, Application of Elovich Equation to the Kinetics of Phosphate Release and Sorption in Soils, Soil Sci. Soc. Am. J. 44 (1980) 265–268. https://doi.org/10.2136/sssaj1980.03615995004400020013x.
[42] Y. Khambhaty, K. Mody, S. Basha, B. Jha, Kinetics, equilibrium and thermodynamic studies on biosorption of hexavalent chromium by dead fungal biomass of marine Aspergillus niger, Chem. Eng. J. 145 (2009) 489–495. https://doi.org/10.1016/j.cej.2008.05.002.
[43] C. Aharoni, D.L. Sparks, S. Levinson, I. Ravina, Kinetics of Soil Chemical Reactions: Relationships between Empirical Equations and Diffusion Models, Soil Sci. Soc. Am. J. 55 (1991) 1307–1312. https://doi.org/10.2136/sssaj1991.03615995005500050019x.
[44] A. Guediri, A. Bouguettoucha, H. Tahraoui, D. Chebli, J. Zhang, A. Amrane, L. Khezami, A.A. Assadi, The Enhanced Adsorption Capacity of Ziziphus jujuba Stones Modified with Ortho-Phosphoric Acid for Organic Dye Removal: A Gaussian Process Regression Approach, Water 16 (2024) 1208.
[45] A. Guediri, A. Bouguettoucha, H. Tahraoui, D. Chebli, A. Amrane, J. Zhang, Thermodynamic study and the development of a support vector machine model for predicting adsorption behavior of orange peel-derived beads in wastewater treatment, J. Mol. Liq. (2024) 124860.
[46] A. Guediri, A. Bouguettoucha, D. Chebli, A. Amrane, The use of encapsulation as a proposed solution to avoid problems encountered with conventional materials in powder form: Application in methylene blue removal from aqueous solutions, J. Mol. Liq. 316 (2020) 113841. https://doi.org/10.1016/j.molliq.2020.113841.
[47] A. Guediri, A. Bouguettoucha, D. Chebli, N. Chafai, A. Amrane, Molecular dynamic simulation and DFT computational studies on the adsorption performances of methylene blue in aqueous solutions by orange peel-modified phosphoric acid, J. Mol. Struct. 1202 (2020) 127290. https://doi.org/10.1016/j.molstruc.2019.127290.
[48] L. Sellaoui, F. Dhaouadi, Z. Li, T.R.S. Cadaval, A.V. Igansi, L.A.A. Pinto, G.L. Dotto, A. Bonilla-Petriciolet, D. Pinto, Z. Chen, Implementation of a multilayer statistical physics model to interpret the adsorption of food dyes on a chitosan film, J. Environ. Chem. Eng. 9 (2021) 105516. https://doi.org/10.1016/j.jece.2021.105516.
[49] H. Xue, X. Gao, M.K. Seliem, M. Mobarak, R. Dong, X. Wang, K. Fu, Q. Li, Z. Li, Efficient adsorption of anionic azo dyes on porous heterostructured MXene/biomass activated carbon composites: Experiments, characterization, and theoretical analysis via advanced statistical physics models, Chem. Eng. J. 451 (2023) 138735. https://doi.org/10.1016/j.cej.2022.138735.
[50] H. Deng, J. Lu, G. Li, G. Zhang, X. Wang, Adsorption of methylene blue on adsorbent materials produced from cotton stalk, Chem. Eng. J. 172 (2011) 326–334. https://doi.org/10.1016/j.cej.2011.06.013.
[51] K.V. Kumar, K. Porkodi, F. Rocha, Isotherms and thermodynamics by linear and non-linear regression analysis for the sorption of methylene blue onto activated carbon: Comparison of various error functions, J. Hazard. Mater. 151 (2008) 794–804. https://doi.org/10.1016/j.jhazmat.2007.06.056.
[52] C. Djama, A. Bouguettoucha, D. Chebli, A. Amrane, H. Tahraoui, J. Zhang, L. Mouni, Experimental and Theoretical Study of Methylene Blue Adsorption on a New Raw Material,

Cynara scolymus—A Statistical Physics Assessment, Sustainability 15 (2023) 10364. https://doi.org/10.3390/su151310364.
[53] A. Geies, G.S. Gomaa, S.M. Ibrahim, A.F. Al-Hossainy, F.K. Abdelwadoud, Experimental and simulated TD-DFT study of malachite green dye and tetrahydroquinoxaline hybrid blend: Its application removal from wastewater, J. Mol. Struct. 1291 (2023) 136050. https://doi.org/10.1016/j.molstruc.2023.136050.
[54] S. Mechati, M. Zamouche, H. Tahraoui, O. Filali, S. Mazouz, I.N.E. Bouledjemer, S. Toumi, Z. Triki, A. Amrane, M. Kebir, Modeling and Optimization of Hybrid Fenton and Ultrasound Process for Crystal Violet Degradation Using AI Techniques, Water 15 (2023) 4274.
[55] H. Tahraoui, A.-E. Belhadj, Z. Triki, N.R. Boudellal, S. Seder, A. Amrane, J. Zhang, N. Moula, A. Tifoura, R. Ferhat, A. Bousselma, N. Mihoubi, Mixed coagulant-flocculant optimization for pharmaceutical effluent pretreatment using response surface methodology and Gaussian process regression, Process Saf. Environ. Prot. 169 (2023) 909–927. https://doi.org/10.1016/j.psep.2022.11.045.
[56] H. Tahraoui, A.-E. Belhadj, A. Amrane, E.H. Houssein, Predicting the concentration of sulfate using machine learning methods, Earth Sci. Inform. (2022) 1–22.
[57] E.H. Houssein, M.R. Saad, F.A. Hashim, H. Shaban, M. Hassaballah, Lévy flight distribution: A new metaheuristic algorithm for solving engineering optimization problems, Eng. Appl. Artif. Intell. 94 (2020) 103731.
[58] I. Harizi, T. Aldahri, D. Chebli, H. Tahraoui, A. Bouguettoucha, S. Rohani, J. Zhang, A. Amrane, Gaussian Process Regression with Levy Flight Optimization: Advanced AR66 Adsorption Studies, Chem. Eng. Res. Des. (2024). https://www.sciencedirect.com/science/article/pii/S0263876224003113 (accessed June 5, 2024).
[59] M. Kebir, I.-K. Benramdhan, N. Nasrallah, H. Tahraoui, N. Bait, H. Benaissa, R. Ameraoui, J. Zhang, A.A. Assadi, L. Mouni, Surface response modeling of homogeneous photo Fenton Fe (III) and Fe (II) complex for sunlight degradation and mineralization of food dye, Catal. Commun. 183 (2023) 106780.
[60] M. Nedjhioui, N. Nasrallah, M. Kebir, H. Tahraoui, R. Bouallouche, A.A. Assadi, A. Amrane, B. Jaouadi, J. Zhang, L. Mouni, Designing an Efficient Surfactant–Polymer–Oil–Electrolyte System: A Multi-Objective Optimization Study, Processes 11 (2023) 1314.
[61] H. Tahraoui, A.-E. Belhadj, A.-E. Hamitouche, Prediction of the Bicarbonate Amount in Drinking Water in the Region of Médéa Using Artificial Neural Network Modelling, Kem. U Ind. Časopis Kemičara Kem. Inženjera Hrvat. 69 (2020) 595–602.
[62] H. Tahraoui, A. Amrane, A.-E. Belhadj, J. Zhang, Modeling the organic matter of water using the decision tree coupled with bootstrap aggregated and least-squares boosting, Environ. Technol. Innov. 27 (2022) 102419. https://doi.org/10.1016/j.eti.2022.102419.
[63] A. Bousselma, D. Abdessemed, H. Tahraoui, A. Amrane, Artificial Intelligence and Mathematical Modelling of the Drying Kinetics of Pre-treated Whole Apricots, Kem. U Ind. 70 (2021) 651–667.
[64] H. Tahraoui, A.-E. Belhadj, N. Moula, S. Bouranene, A. Amrane, Optimisation and Prediction of the Coagulant Dose for the Elimination of Organic Micropollutants Based on Turbidity, Kem. U Ind. 70 (2021) 675–691.
[65] H. Tahraoui, S. Toumi, A.H. Hassein-Bey, A. Bousselma, A.N.E.H. Sid, A.-E. Belhadj, Z. Triki, M. Kebir, A. Amrane, J. Zhang, Advancing Water Quality Research: K-Nearest Neighbor Coupled with the Improved Grey Wolf Optimizer Algorithm Model Unveils New Possibilities for Dry Residue Prediction, Water 15 (2023) 2631.
[66] H. Tahraoui, A.-E. Belhadj, A. -e Hamitouche, M. Bouhedda, A. Amrane, Predicting the concentration of sulfate (So4 2–) in drinking water using artificial neural networks: A case study: Médéa-algeria, Desalination Water Treat. 217 (2021) 181–194.
[67] M. Zamouche, H. Tahraoui, Z. Laggoun, S. Mechati, R. Chemchmi, M.I. Kanjal, A. Amrane, A. Hadadi, L. Mouni, Optimization and prediction of stability of emulsified liquid membrane (ELM): Artificial neural network, Processes 11 (2023) 364.

[68] H. TAHRAOUI, A.-E. Belhadj, Optimisation de l'élimination des micropolluants organiques, 2021.
[69] M.M. Yahoum, S. Toumi, S. Hentabli, H. Tahraoui, S. Lefnaoui, A. Hadjsadok, A. Amrane, M. Kebir, N. Moula, A.A. Assadi, Experimental Analysis and Neural Network Modeling of the Rheological Behavior of Xanthan Gum and Its Derivatives, Materials 16 (2023) 2565.
[70] M. Kebir, I. kahina Benramdhan, N. Noureddine, H. Tahraoui, B. Nadia, B. Houssine, A. Rachid, J. Zhang, A.A. ASSADI, L. Mouni, Sunlight Degradation and Mineralization of Food Dye Photoinduced by Homogenous Photo Fenton Fe (III) and Fe (II)/Complex: Surface Response Modeling, (2023).
[71] C. Djama, A. Bouguettoucha, D. Chebli, A. Amrane, H. Tahraoui, J. Zhang, L. Mouni, Experimental and Theoretical Study of Methylene Blue Adsorption on a New Raw Material, Cynara scolymus—A Statistical Physics Assessment, Sustainability 15 (2023) 10364. https://doi.org/10.3390/su151310364.
[72] S. Shrestha, Chemical, Structural and Elemental Characterization of Biosorbents Using FE-SEM, SEM-EDX, XRD/XRPD and ATR-FTIR Techniques, J. Chem. Eng. Process Technol. 7 (2016). https://doi.org/10.4172/2157-7048.1000295.
[73] R. Dod, G. Banerjee, S. Saini, Adsorption of methylene blue using green pea peels (Pisum sativum): A cost-effective option for dye-based wastewater treatment, Biotechnol. Bioprocess Eng. 17 (2012) 862–874. https://doi.org/10.1007/s12257-011-0614-5.
[74] A. Shoaib, Nafisa, G. Riaz, Q. Fatima, U. Fatima, N. Iqbal, FOURIER-TRANSFORM INFRARED SPECTROSCOPY IDENTIFIED CHANGES IN THE CELL WALL COMPONENTS ASSOCIATED WITH THE SIMULTANEOUS TRAFFICKING OF WHITE MOLD FUNGUS AND COPPER, Pak. J. Phytopathol. 34 (2022) 193–200. https://doi.org/10.33866/phytopathol.034.02.0795.
[75] T.M. Eldeeb, U.O. Aigbe, K.E. Ukhurebor, R.B. Onyancha, M.A. El-Nemr, M.A. Hassaan, S. Ragab, O.A. Osibote, A. El Nemr, Adsorption of methylene blue (MB) dye on ozone, purified and sonicated sawdust biochars, Biomass Convers. Biorefinery 14 (2024) 9361–9383. https://doi.org/10.1007/s13399-022-03015-w.
[76] T.A. Khan, R. Rahman, I. Ali, E.A. Khan, A.A. Mukhlif, Removal of malachite green from aqueous solution using waste pea shells as low-cost adsorbent – adsorption isotherms and dynamics, Toxicol. Environ. Chem. 96 (2014) 569–578. https://doi.org/10.1080/02772248.2014.969268.
[77] O.O. Namal, E. Kalipci, Adsorption kinetics of methylene blue using alkali and microwave-modified apricot stones, Sep. Sci. Technol. 54 (2019) 1722–1738. https://doi.org/10.1080/01496395.2018.1541469.
[78] C. Djama, A. Bouguettoucha, D. Chebli, A. Amrane, H. Tahraoui, J. Zhang, L. Mouni, Experimental and Theoretical Study of Methylene Blue Adsorption on a New Raw Material, Cynarascolymus - A statistical Physics Assessment, Engineering, 2023. https://doi.org/10.20944/preprints202305.0418.v1.
[79] D. Blau, L. Bach, M. Scott, S. Rubin, Clark Moustakas (1923–2012): Scholar, teacher, colleague and friend., Humanist. Psychol. 41 (2013) 97–99. https://doi.org/10.1080/08873267.2013.752695.
[80] O. Amrhar, L. El Gana, M. Mobarak, Calculation of adsorption isotherms by statistical physics models: a review, Environ. Chem. Lett. 19 (2021) 4519–4547. https://doi.org/10.1007/s10311-021-01279-8.
[81] M. Ben Yahia, M. Tounsi, F. Aouaini, S. Knani, M. Ben Yahia, A. Ben Lamine, A statistical physics study of the interaction of [7]-helicene with alkali cations (K^+ and Cs^+): new insights on microscopic adsorption behavior, RSC Adv. 7 (2017) 44712–44723. https://doi.org/10.1039/C7RA08387D.
[82] L. Sellaoui, H. Guedidi, S. Knani, L. Reinert, L. Duclaux, A. Ben Lamine, Application of statistical physics formalism to the modeling of adsorption isotherms of ibuprofen on activated carbon, Fluid Phase Equilibria 387 (2015) 103–110. https://doi.org/10.1016/j.fluid.2014.12.018.
[83] S. Mahmoudi, Z. Chemat-Djenni, A. Bouguettoucha, A. Guediri, D. Chebli, A. Gil, Removal of Pb (II) from aqueous solutions by new layered double hydroxides adsorbent MgCuCaAl-LDH: Free

Gibbs energy, entropy and internal energy studies, Inorg. Chem. Commun. 144 (2022) 109910. https://doi.org/10.1016/j.inoche.2022.109910.
[84] A. Yazidi, L. Sellaoui, G.L. Dotto, A. Bonilla-Petriciolet, A.C. Fröhlich, A.B. Lamine, Monolayer and multilayer adsorption of pharmaceuticals on activated carbon: Application of advanced statistical physics models, J. Mol. Liq. 283 (2019) 276–286. https://doi.org/10.1016/j.molliq.2019.03.101.
[85] D. Chaker, A. Bouguettoucha, C. Derradji, A. Amrane, H. Tahraoui, J. Zhang, L. Mouni, Experimental and Theoretical Study of Methylene Blue Adsorption on a New Raw Material, Cynarascolymus - A statistical Physics Assessment, 2023. https://doi.org/10.20944/preprints202305.0418.v1.
[86] A. Guediri, A. Bouguettoucha, D. Chebli, N. Chafai, A. Amrane, Molecular dynamic simulation and DFT computational studies on the adsorption performances of methylene blue in aqueous solutions by orange peel-modified phosphoric acid, J. Mol. Struct. 1202 (2020) 127290. https://doi.org/10.1016/j.molstruc.2019.127290.
[87] A. Hadadi, A. Imessaoudene, J.-C. Bollinger, A. Bouzaza, A. Amrane, H. Tahraoui, L. Mouni, Aleppo pine seeds (Pinus halepensis Mill.) as a promising novel green coagulant for the removal of Congo red dye: Optimization via machine learning algorithm, J. Environ. Manage. 331 (2023) 117286.
[88] N. Somsesta, C. Piyamawadee, V. Sricharoenchaikul, D. Aht-Ong, Adsorption isotherms and kinetics for the removal of cationic dye by Cellulose-based adsorbent biocomposite films, Korean J. Chem. Eng. 37 (2020) 1999–2010. https://doi.org/10.1007/s11814-020-0602-6.
[89] A.A. Babaei, A. Khataee, E. Ahmadpour, M. Sheydaei, B. Kakavandi, Z. Alaee, Optimization of cationic dye adsorption on activated spent tea: Equilibrium, kinetics, thermodynamic and artificial neural network modeling, Korean J. Chem. Eng. 33 (2016) 1352–1361. https://doi.org/10.1007/s11814-014-0334-6.
[90] S. Chen, C. Qin, T. Wang, F. Chen, X. Li, H. Hou, M. Zhou, Study on the adsorption of dyestuffs with different properties by sludge-rice husk biochar: Adsorption capacity, isotherm, kinetic, thermodynamics and mechanism, J. Mol. Liq. 285 (2019) 62–74. https://doi.org/10.1016/j.molliq.2019.04.035.
[91] R.K. Ghosh, D.P. Ray, S. Debnath, A. Tewari, I. Das, Optimization of process parameters for methylene blue removal by jute stick using response surface methodology, Environ. Prog. Sustain. Energy 38 (2019) 13146. https://doi.org/10.1002/ep.13146.
[92] M. Danish, T. Ahmad, W.N.A.W. Nadhari, M. Ahmad, W.A. Khanday, L. Ziyang, Z. Pin, Optimization of banana trunk-activated carbon production for methylene blue-contaminated water treatment, Appl. Water Sci. 8 (2018) 9. https://doi.org/10.1007/s13201-018-0644-7.
[93] K.N. Aboua, Y.A. Yobouet, K.B. Yao, D.L. Goné, A. Trokourey, Investigation of dye adsorption onto activated carbon from the shells of Macoré fruit, J. Environ. Manage. 156 (2015) 10–14. https://doi.org/10.1016/j.jenvman.2015.03.006.